Monthly Notices of the ROYAL ASTRONOMICAL SOCIETY

MNRAS **497,** 2569–2585 (2020) doi:10.1093/mnras/staa2104
Advance Access publication 2020 July 20

X-ray spectroscopy of the γ-ray brightest nova V906 Car (ASASSN-18fv)

Kirill V. Sokolovsky [1,2,3★] Koji Mukai,[4] Laura Chomiuk,[1] Raimundo Lopes de Oliveira,[5,6] Elias Aydi,[1] Kwan-Lok Li,[7] Elad Steinberg,[8] Indrek Vurm,[9] Brian D. Metzger,[8] Adam Kawash,[1] Justin D. Linford,[10] Amy J. Mioduszewski,[10] Thomas Nelson,[11] Jan-Uwe Ness,[12] Kim L. Page [13] Michael P. Rupen,[14] Jennifer L. Sokoloski[8] and Jay Strader[1]

[1]*Department of Physics and Astronomy, Center for Data Intensive and Time Domain Astronomy, Michigan State University, 567 Wilson Rd, East Lansing, MI 48824, USA*
[2]*Sternberg Astronomical Institute, Moscow State University, Universitetskii pr. 13, 119992 Moscow, Russia*
[3]*Astro Space Center of Lebedev Physical Institute, Profsoyuznaya St 84/32, 117997 Moscow, Russia*
[4]*CRESST and X-ray Astrophysics Laboratory, NASA/GSFC, Greenbelt, MD 20771, USA*
[5]*Departamento de Física, Universidade Federal de Sergipe, Av. Marechal Rondon, S/N, 49000-000 São Cristóvão, SE, Brazil*
[6]*Observatório Nacional, Rua Gal. José Cristino 77, 20921-400 Rio de Janeiro, RJ, Brazil*
[7]*Institute of Astronomy, National Tsing Hua University, Hsinchu 30013, Taiwan*
[8]*Department of Physics and Columbia Astrophysics Laboratory, Columbia University, New York, NY 10027, USA*
[9]*Tartu Observatory, University of Tartu, Tõravere, 61602 Tartumaa, Estonia*
[10]*National Radio Astronomy Observatory, Domenici Science Operations Center, 1003 Lopezville Road, Socorro, NM 87801, USA*
[11]*Department of Physics and Astronomy, University of Pittsburgh, Pittsburgh, PA 15260, USA*
[12]*XMM-Newton Observatory SOC, European Space Astronomy Centre, Camino Bajo del Castillo s/n, Urb. Villafranca del Castillo, E-28692 Villanueva de la Cañada, Madrid, Spain*
[13]*School of Physics and Astronomy, University of Leicester, University Road, Leicester LE1 7RH, UK*
[14]*National Research Council, Herzberg Astronomy and Astrophysics, 717 White Lake Rd, PO Box 248, Penticton, BC V2A 6J9, Canada*

Accepted 2020 July 14. Received 2020 July 14; in original form 2020 April 13

ABSTRACT

Shocks in γ-ray emitting classical novae are expected to produce bright thermal and non-thermal X-rays. We test this prediction with simultaneous *NuSTAR* and *Fermi*/LAT observations of nova V906 Car, which exhibited the brightest GeV γ-ray emission to date. The nova is detected in hard X-rays while it is still γ-ray bright, but contrary to simple theoretical expectations, the detected 3.5–78 keV emission of V906 Car is much weaker than the simultaneously observed >100 MeV emission. No non-thermal X-ray emission is detected, and our deep limits imply that the γ-rays are likely hadronic. After correcting for substantial absorption ($N_{\rm H} \approx 2 \times 10^{23}$ cm^{-2}), the thermal X-ray luminosity (from a 9 keV optically thin plasma) is just ∼2 per cent of the γ-ray luminosity. We consider possible explanations for the low thermal X-ray luminosity, including the X-rays being suppressed by corrugated, radiative shock fronts or the X-rays from the γ-ray producing shock are hidden behind an even larger absorbing column ($N_{\rm H} > 10^{25}$ cm^{-2}). Adding *XMM–Newton* and *Swift*/XRT observations to our analysis, we find that the evolution of the intrinsic X-ray absorption requires the nova shell to be expelled 24 d after the outburst onset. The X-ray spectra show that the ejecta are enhanced in nitrogen and oxygen, and the nova occurred on the surface of a CO-type white dwarf. We see no indication of a distinct supersoft phase in the X-ray light curve, which, after considering the absorption effects, may point to a low mass of the white dwarf hosting the nova.

Key words: white dwarfs – novae, cataclysmic variables.

1 INTRODUCTION

1.1 X-ray emission of classical novae

A nova explosion is powered by nuclear fusion that ignites at the bottom of a hydrogen-rich shell on the surface of an accreting white dwarf in a binary star system (Bode & Evans 2008; Starrfield, Iliadis & Hix 2016). Recent summaries of their observational appearance across the electromagnetic spectrum were presented by Poggiani (2018) and Della Valle & Izzo (2020). Specifically, the X-ray emission is produced during the following stages of a nova event (Krautter 2008; Hernanz & Sala 2010; Mukai 2017):

(i) A soft X-ray flash should be produced by the optically thick ejecta (i.e. 'fireball') during the first hours of explosion, before the fireball expands and cools sufficiently to shift the peak of its emission from X-ray to UV and optical bands (Schwarz et al. 2001; Krautter 2002; Ness et al. 2007). So far, the attempts to observe the fireball X-ray emission have not resulted in an unambiguous detection (Kato et al. 2016; Morii et al. 2016). Morii et al. (2013) interpret the X-ray transient MAXI J0158–744 as the nova fireball, while Li et al. (2012) suggest the X-rays are produced by interaction of the nova shell with

★ E-mail: kirx@kirx.net

the Be-type donor wind. The ongoing all-sky X-ray surveys with MAXI/GSC (Negoro et al. 2016) and SRG/eROSITA (Merloni et al. 2012; Predehl et al. 2016) have a chance to detect a nova fireball.

(ii) Hard X-ray emission (∼1–10 keV) is produced by optically thin plasma compressed and heated by internal shocks in the nova outflow and is often observed days to month after explosion (O'Brien, Lloyd & Bode 1994; Mukai et al. 2014).

(iii) Supersoft (<0.5 keV, SSS) optically thick thermal X-ray emission from the atmosphere of the nuclear-burning white dwarf is often observed when the nova ejecta become transparent to soft X-rays weeks-to-months after the explosion (Hasinger 1994; Kahabka & van den Heuvel 1997; Schwarz et al. 2011).

(iv) Line-dominated emission from the shock-heated plasma may persist after the supersoft emission fades (Rohrbach, Ness & Starrfield 2009; Drake et al. 2014).

(v) When accretion restarts after the nova explosion, X-ray emission is produced in the region where accreting matter hits the white dwarf (the boundary layer between the disc and the surface in non-magnetic white dwarfs or the accreting column in magnetic ones). This is the accretion-powered X-ray emission found in cataclysmic variables (Takei et al. 2011; Mukai 2017).

The X-ray emission, including that powered by shocks, is widely assumed to be thermal. However, detection of continuum GeV γ-ray emission from novae (Abdo et al. 2010; Ackermann et al. 2014; Cheung et al. 2016; Franckowiak et al. 2018) implies efficient particle acceleration by shocks (e.g. Blandford 1994; Caprioli & Spitkovsky 2014; Slane et al. 2015). The accelerated particles produce γ-rays through the hadronic (pion production and decay) and/or leptonic (direct acceleration of electrons and inverse Compton scattering of ambient photons or relativistic bremsstrahlung) mechanisms (Metzger et al. 2015; Martin et al. 2018) – the same mechanisms invoked to explain high-energy emission from jetted active galactic nuclei known as 'blazars' (Boettcher 2010). If the hadronic scenario is responsible for the γ-ray production, novae should be sources of neutrinos that may be reachable for the next generation detectors (Metzger et al. 2016). In both hadronic and leptonic models, the relativistic particles may also contribute to non-thermal emission in X-rays (Vurm & Metzger 2018) and emit synchrotron radiation in the radio band (Vlasov, Vurm & Metzger 2016).

It is also possible to produce non-thermal X-rays through Compton degradation of MeV line emission from decaying radioactive isotopes such as ^{22}Na (Suzuki & Shigeyama 2010, see also references in Orio et al. 2001 and the discussion in Section 2.1). The MeV line emission has long been predicted, but never observed (Hernanz & José 2006; Hernanz 2014; Jose 2016).

The X-ray emission is absorbed by the expanding nova ejecta and, to an usually lesser extent, by the interstellar medium. The contributions of intrinsic and interstellar absorption may be disentangled as the intrinsic absorption decreases with time as the nova ejecta disperse (e.g. Mukai & Ishida 2001; Page et al. 2015). The time it takes for the nova ejecta to thin out and reveal the underlying SSS may be used (together with the expansion velocity determined from optical spectroscopy) to estimate the nova ejecta mass (Schwarz et al. 2011; Henze et al. 2014).

1.2 X-rays from γ-ray detected novae

Surprisingly, no X-rays below 10 keV (the energy band where most X-ray observatories, including *Swift/XRT* and *XMM–Newton*, operate) have been observed from classical novae (i.e. novae with dwarf companions), while the novae were detected in γ-rays (Metzger et al. 2014, Gordon et al., in preparation). This might be explained if the soft X-rays are absorbed by the dense nova ejecta in the first weeks following explosion (see Section 3.3). Interestingly, novae with red giant donors, like V407 Cyg, are detected in X-rays simultaneously with the GeV emission, likely due to the shock being external – between the ejecta and the giant companion's wind – rather than internal to the nova ejecta (Nelson et al. 2012; Orlando & Drake 2012).

Because of its high sensitivity above 10 keV, *Nuclear Spectroscopic Telescope Array* (*NuSTAR*; Section 1.3) can penetrate dense nova ejecta and constrain the X-ray luminosity simultaneously with the GeV detection by *Fermi*/Large Area Telescope (LAT). V339 Del and V5668 Sgr were the first classical novae observed with *NuSTAR* while they were still bright in GeV γ-rays (Section 3.4); contrary to expectation, both resulted in non-detections (Mukai et al., in preparation). The first detection of X-rays simultaneous with γ-rays for a classical nova finally came with V5855 Sgr, but deepened the mystery of the missing X-rays (Nelson et al. 2019). Observed 12 d after eruption, the X-rays were consistent with highly absorbed thermal plasma (see e.g. Ghisellini 2013), and the ratio of unabsorbed X-ray to γ-ray luminosity was $L_{20\,\mathrm{keV}}/L_{100\,\mathrm{MeV}} \approx 0.01$ (monochromatic flux ratio in νF_ν units; Section 3.4). This ratio was surprisingly low because we expect only a small fraction ($\lesssim$10 per cent) of the shock energy to be transferred to the γ-ray emitting non-thermal particles (see Section 3.4.2 and Metzger et al. 2015). Meanwhile, the shocks in novae are predicted to be dense and radiative, implying that the bulk of the shock energy should be efficiently radiated away, and the shock speeds of $\gtrsim$1000 km s^{-1} imply that the bulk of this thermal emission should emerge in the X-ray band (Metzger et al. 2014, 2015). A possible explanation for the low value of $L_{20\,\mathrm{keV}}/L_{100\,\mathrm{MeV}}$ in V5855 Sgr is suppression of X-rays at nova shock fronts (Nelson et al. 2019). If the shocks are dense and radiative, the shock front becomes subject to instabilities and develops a corrugated structure that can lead to post-shock temperatures a factor of 4–36 lower than expected (Steinberg & Metzger 2018). In that case, the shock luminosity is expected to emerge at longer wavelengths (i.e. optical/infrared; Metzger et al. 2014; Steinberg & Metzger 2020). Notably, correlated variations between the optical and γ-ray light curves of novae have now been observed in two (possibly three; Munari, Hambsch & Frigo 2017) systems – including the subject of this paper, V906 Car – supporting this model (Li et al. 2017; Aydi et al. 2020).

Was the low value of $L_{20\,\mathrm{keV}}/L_{100\,\mathrm{MeV}}$ in V5855 Sgr unusual amongst novae? We know that the γ-ray properties of novae are diverse, with >100 MeV luminosities spanning at least a factor of ∼30 (Franckowiak et al. 2018). And yet, we do not understand the cause of this diversity, or the full range of conditions in nova shocks. These open questions led us to observe V906 Car with *NuSTAR* while it was detected with *Fermi*/LAT – the results of which we present here.

1.3 Orbital observatories

Our current understanding of nova X-ray emission comes primarily from *XMM–Newton* (e.g. Hernanz & Sala 2005) and *Swift* (Ness et al. 2007; Schwarz et al. 2011; Ness 2012) observations. *NuSTAR* has high sensitivity to very hard X-rays and is just starting to reveal the behaviour of novae above 10 keV. *Fermi*/LAT detection of GeV emission from V407 Cyg (Abdo et al. 2010) sparked a renewed interest in novae. Here, we briefly summarize the technical capabilities of these space missions.

The *NuSTAR* (Harrison et al. 2013b) was launched into a low-Earth orbit on 2012 June 13, equipped with two identical focusing X-ray telescopes (XRTs) sensitive to photons with energies 3–79 keV (Madsen et al. 2015). It provides two orders of magnitude higher

sensitivity (and an order of magnitude higher angular resolution) compared to the coded aperture mask instruments *Swift*/Burst Alert Telescope (BAT) and *INTEGRAL* sensitive to this energy range. Its exceptional sensitivity makes new classes of objects, including classical novae, accessible for study in the hard X-ray regime. The 10 m-long extendible mast separating the X-ray optics and detector units limits the speed at which the observatory can repoint, so *NuSTAR* performs long observations of a single field interrupted by the Earth occultations, before repointing to another field (much like the *Hubble Space Telescope*).

The *Neil Gehrels Swift Observatory (Swift)* has been operating in low-Earth orbit since 2004 November 20 (Gehrels et al. 2004). While originally designed for observations of γ-ray bursts and their afterglows, it became an essential tool for multiwavelength studies across various branches of astronomy. Its unique ability to quickly repoint makes it practical to perform monitoring observations of multiple sources and allows *Swift* to use efficiently its time for observations (except for the South Atlantic Anomaly passages), switching to a new target when the previous one goes into Earth occultation. *Swift* is equipped with the coded aperture mask, wide field-of-view BAT (Barthelmy et al. 2005) collecting very hard 15–150 keV X-rays, the focusing XRT (Burrows et al. 2005) being sensitive to 0.3–10 keV X-rays, and the Ultraviolet/Optical Telescope (UVOT; Roming et al. 2005).

XMM–Newton was launched on 1999 December 10 into a highly elliptical orbit allowing for long uninterrupted observations (Jansen et al. 2001). The observatory can perform high-resolution X-ray grating spectroscopy in the range 0.33–2.1 keV (6–38 Å) using its reflection grating spectrometer (RGS) instruments (den Herder et al. 2001). It is also equipped for traditional medium-resolution spectroscopy with a pair of EPIC-MOS[1] and the EPIC-pn[2] imaging cameras covering a wider energy range of 0.2–10 keV. The EPIC-MOS and EPIC-pn cameras differ in the detector array geometry, electronics (resulting in different readout times), and quantum efficiency (front- and back-illuminated design, respectively). The observatory also operates the Optical Monitor telescope (Mason et al. 2001) that is similar to the *Swift*/UVOT. All *XMM–Newton* instruments are normally operating simultaneously (the photons not intercepted by the RGS gratings are collected by the EPIC-MOS cameras, while the EPIC-pn camera is fed by its own X-ray mirror assembly).

Fermi Gamma-ray Space Telescope was launched into low-earth orbit on 2008 June 11. Its main instrument, the (LAT; Abdo et al. 2009; Atwood et al. 2009; Ackermann et al. 2012) is a pair-conversion detector sensitive to γ-rays in the energy range 20 MeV–300 GeV. Its collecting area and 2.4 sr field of view are far superior to the contemporary GeV telescopes AGILE (Tavani et al. 2008, 2009) and DAMPE (Chang et al. 2017) and their predecessor – EGRET, the spark chamber detector on board the *Compton* Gamma Ray Observatory (Thompson et al. 1993). *Fermi*/LAT normally performs an all-sky survey every day, but see Section 2.7.

1.4 V906 Car (2018)

V906 Car (Nova Carinae 2018, ASASSN-18fv) was discovered on 2018 March 20.32 UT (Stanek et al. 2018) by the ASAS-SN survey (Shappee et al. 2014; Kochanek et al. 2017) as a new saturated object (<10 mag) near the Carina Nebula. No previous outbursts were found by ASAS-SN or among the numerous amateur images of the Carina region (Toumilovitch, Blane & Rijsdijk 2018). The initial spectroscopic observations by Strader et al. (2018) on March 21 and Izzo et al. (2018) on March 22 were unable to distinguish between the possibilities of the object being a classical nova, a luminous red nova (e.g. Pastorello et al. 2019), or a young stellar object outburst (e.g. Hartmann & Kenyon 1996). The main source of confusion were the low velocities derived from the emission lines at early times. Luckas (2018) obtained another spectrum on March 21 and interpreted it as that of a classical nova in the iron curtain phase. The infrared spectrum obtained by Rabus & Prieto (2018) on April 1 was consistent with a Fe II-type nova, according to the classification scheme of Williams (1992).

By a lucky coincidence, V906 Car was within the field of view of the BRITE cubesat constellation (Weiss et al. 2014; Pablo et al. 2016; Popowicz et al. 2017), as it was performing photometry of a nearby red giant HD 92063 (see also Sections 2.3 and 2.4; Kuschnig et al. 2018). We adopt $t_0 = 2018$ March 16.13 UTC (HJD2458193.63) as the nova explosion time derived from the BRITE light curve by (Aydi et al. 2020, see their Supplementary fig. 2). The adopted t_0 is consistent with the reported non-detection by Evryscope 2 h earlier (Corbett et al. 2018). The optical light curve of V906 Car, peaking at 5.9 mag, showed an unusual series of fast flares superimposed on the slowly evolving nova light curve.

As of 2020 June, V906 Car is the brightest γ-ray nova observed by *Fermi*/LAT to date (Jean et al. 2018), reaching peak 0.1–300 GeV flux of $(1.91 \pm 0.20) \times 10^{-6}$ photons cm^{-2} s^{-1} in a 12 h integration centred on 2018 April 14.25 UT ($t_0 + 29$ d; Section 2.7; Aydi et al. 2020). Remarkably, a series of distinct flares was resolved in the *Fermi*/LAT light curve that coincided with the optical flares observed by BRITE. This led Aydi et al. (2020) to conclude that these flares are manifestations of shocks. V906 Car was also the first nova detected by the *AGILE* mission (Piano et al. 2018) observing at the >100 MeV band similar to *Fermi*/LAT.

V906 Car was observed by *INTEGRAL* starting on 2018 April 23 ($t_0 + 38$ d), with the aim of searching for the MeV γ-ray nucleosynthesis lines predicted in novae,[3] one of the long-standing goals of the *INTEGRAL* mission (Hernanz et al. 2002; Siegert et al. 2018). No MeV line detections were reported. High-cadence optical photometry was obtained with *INTEGRAL*/OMC, revealing variations of up to 0.3 mag on time-scales of several hours to one day (Domingo et al. 2018).

McLoughlin, Blundell & Lee (2020) report dense monitoring of Fe II and [O I] features in the optical spectrum of V906 Car. The authors argue that these spectral features might be originating in a rotating circumbinary disc. Pavana et al. (2020) also report spectroscopy of V906 Car concluding that the nova ejecta are clumpy and have an overall asymmetric bipolar geometry.

V906 Car was also observed at radio wavelengths with the Australia Telescope Compact Array resulting in an initial non-detection on 2018 April 03 ($t_0 + 18$ d; Ryder, Kool & Chomiuk 2018). The mJy-level radio emission was detected first on 2018 May 13 ($t_0 + 58$ d) and reached its peak in late 2019 (Aydi et al. 2020).

Hard X-ray emission from V906 Car was detected by *NuSTAR*, and preliminary results were reported in Nelson et al. (2018) and Aydi et al. (2020). Here, we present a more in-depth look at the X-ray emission from this nova, analysing the *NuSTAR* data together with *XMM–Newton* and *Swift* observations.

[1]European Photon Imaging Camera – Metal Oxide Semiconductor (Turner et al. 2001).

[2]European Photon Imaging Camera with the pn-type detector (Strüder et al. 2001).

[3]https://www.cosmos.esa.int/web/integral/news-2018

Table 1. *NuSTAR* observing log.

ObsID	Epoch (d)	Start UT	Stop UT	Exposure FPMA (ks)	Exposure FPMB (ks)	Net count rate FPMA (cts s^{-1})	Net count rate FPMB (cts s^{-1})
80301306002	36	2018-04-20 14:46	2018-04-22 02:01	48.8	48.5	0.0158 ± 0.0007	0.0163 ± 0.0007
90401322002	57	2018-05-11 16:26	2018-05-12 18:01	47.5	47.4	0.0434 ± 0.0010	0.0418 ± 0.0010

Note. Column designation: Column 1 – observation identification number; Column 2 – time since outburst; Columns 3 and 4 – start and stop time of the observation (interrupted by the Earth occultations and South Atlantic Anomaly passes); Columns 5 and 6 – total on-source exposure time for FPMA and FPMB, respectively; Columns 7 and 8 – source count rate (background-subtracted) for FPMA and FPMB, respectively.

1.5 Galactic extinction towards V906 Car

Optical spectroscopy allowed Aydi et al. (2020) to estimate the interstellar reddening towards V906 Car using the diffuse interstellar bands (Friedman et al. 2011) and the Na I D absorption features (Poznanski, Prochaska & Bloom 2012). Combining these two methods, the authors found $E(B-V) = 0.36 \pm 0.05$. Assuming the standard value of $R_V = 3.1 = A_V/E(B-V)$ (Schultz & Wiemer 1975), this corresponds to a V-band extinction of $A_V = 1.12$ mag.

An alternative method of estimating extinction to a nova is based on the typical intrinsic colour of $(B-V)_0 = -0.02$ when the nova is two magnitudes below its peak [the dispersion of $(B-V)_0$ is 0.12 mag, van den Bergh & Younger 1987]. The nova light at this stage may be dominated by optically thick free–free (blackbody) emission (Hachisu & Kato 2014). According to Aydi et al. (2020), for V906 Car the observed $(B-V) = 0.23$ around $t_0 + 55$ d, corresponding to a colour excess of $E(B-V) = 0.25$ – consistent with the spectroscopically derived value within 1σ uncertainty of the intrinsic colour. We adopt the spectroscopically derived $E(B-V)$ as it has lower uncertainty. It is also not clear whether the method based on intrinsic colour is applicable to V906 Car, considering the major contribution of shock-powered optical emission (Aydi et al. 2020).

We note that Pavana et al. (2020), relying on a different Na I D equivalent width-reddening calibration and the expected nova colour around maximum light, arrive at a much higher $E(B-V)$ value. This value, however, would imply the Galactic X-ray absorbing column is much higher than that we derive from *XMM–Newton* observations, as described in Section 2.3.

To estimate the expected Galactic X-ray absorbing column to V906 Car, we utilize the relation proposed by Güver & Özel (2009) between the optical extinction and the hydrogen column density:

$$N_{\rm H} = 2.21 \times 10^{21}\ {\rm cm}^{-2} \times A_V = 2.47 \times 10^{21}\ {\rm cm}^{-2}. \quad (1)$$

This value should be a lower limit on the total X-ray absorbing column, as the nova ejecta produce large intrinsic absorption (Section 3.3). The derived $N_{\rm H}$ is consistent with the value derived from our late-time *XMM–Newton* spectroscopy (Table 3). The total H I column density in the direction of V906 Car derived from Galactic surveys of the 21 cm emission line is $N_{\rm HI} = 1.29 \times 10^{22}$ cm^{-2} (Bajaja et al. 2005; Kalberla et al. 2005), so the nova is in front of 80 per cent of the Galactic absorbing column. Comparison of the A_V estimated for V906 Car to the total optical V-band extinction in its direction (3.6 mag; Schlafly & Finkbeiner 2011) also suggests that the nova is nearby. Aydi et al. (2020) adopted a distance to V906 Car of 4 kpc based on the uncertain *Gaia* parallax measurement (Bailer-Jones et al. 2018) and the Galactic 3D extinction map of Chen et al. (2019).

1.6 Scope of this work

We present a joint analysis of *NuSTAR*, *XMM–Newton*, *Swift*, and *Fermi* observations of V906 Car. We fit the model describing the observed X-ray spectra and constrain the elemental abundances in the nova ejecta. We compare the simultaneous hard X-ray (*NuSTAR*) and γ-ray (*Fermi*/LAT) observations to identify the physical origin of the high-energy emission in this nova, and discuss the possible location of the X-ray emitting shock. In Section 2, we describe the observations of V906 Car performed with the instruments introduced in Section 1.3. In Section 3, we estimate physical parameters of the nova, and summarize our findings in Section 4.

Throughout this paper, we adopt a significance level $\alpha_{\rm lim} = 0.05$: we reject spectral models that have a probability $p > \alpha_{\rm lim}$ of obtaining the observed or a more extreme value of the test statistic by chance.[4] We use χ^2 as the test statistic as we deal with well-sampled spectra (Section 2.1). We express the abundances of the chemical elements by the number of atoms relative to the number of hydrogen atoms following the `XSPEC` convention (Section 3.1). The quoted uncertainties of the model parameters are at 1σ level. For power-law emission, we define the spectral index α as $F_\nu \propto \nu^\alpha$, where F_ν is the spectral flux density and ν is the frequency; meanwhile the corresponding index in the distribution of the number of incoming photons as a function of energy is ${\rm d}N(E)/{\rm d}E \propto E^{-\Gamma}$, where Γ is called the photon index and $\Gamma = 1 - \alpha$. The same power law expressed in spectral energy distribution units (Gehrels 1997) is $\nu F_\nu \propto \nu^{\alpha+1} \propto \nu^{-\Gamma+2}$. When referring to 'GeV γ-rays' we imply emission in the *Fermi*/LAT band (0.1–300 GeV).

2 OBSERVATIONS AND ANALYSIS

2.1 *NuSTAR* spectroscopy

NuSTAR observed V906 Car during two epochs: $t_0 + 36$ and $t_0 + 57$ d. The nova is clearly detected with 1563 and 4046 counts in the source region (two focal plane modules combined) in the first and second epoch, respectively. The observing log is presented in Table 1. We use `nupipeline` and `nuproducts` commands from `HEASoft 6.26.1` to extract source and background spectra from the focal plane modules A (FPMA) and B (FPMB). A circular extraction region with radius of 30 arcsec was centred on the X-ray image of the nova using `ds9` (Joye & Mandel 2003). The centring was done for FPMA and FPMB event files separately. The background was extracted from five circular regions of the same size that were manually placed near the nova on the same CZT (Arnaud, Smith & Siemiginowska 2011) chip. We checked that the specific choice of the background region does not affect the results. We use `grppha` to mark channels 0–46 and 1910–4095 as 'bad', restricting the energy range to 3.5–78.0 keV and grouping the source spectra to contain at least 25 counts per bin. The spectra together with the redistribution matrix (RMF; describes the probability of a count being registered at a certain energy channel as a function of the photon energy) and auxiliary response (ARF; describes the detector

[4] See e.g. Chapter 5 of Wall & Jenkins (2003) and https://en.wikipedia.org/wiki/P-value.

Table 2. Parameters of *NuSTAR* spectral fits.

$t - t_0$ (d)	vphabs N_H (10^{22} cm^{-2})	kT (keV)	FeCoNi abundances	CNO abundances	C_{FPMB}	3.5–78.0 keV Flux $\log_{10}$(erg cm^{-2} s^{-1})	3.5–78.0 keV Flux$_0$ $\log_{10}$(erg cm^{-2} s^{-1})
Solar abundances model: $\chi^2_{red} = 3.1047$, d.o.f. $= 200$, $p = 0.00$							
36	165 ± 14	13.7 ± 1.7	1.0	1.0	1.23 ± 0.08	−11.570 ± 0.012	−11.068 ± 0.012
57	16.4 ± 1.6	7.5 ± 0.3	—'—	—'—	1.01 ± 0.04	−11.454 ± 0.007	−11.179 ± 0.007
Fe-deficient model: $\chi^2_{red} = 1.0281$, d.o.f. $= 199$, $p = 0.38$							
36	293 ± 20	8.0 ± 0.9	0.09 ± 0.03	1.0	1.11 ± 0.06	−11.570 ± 0.012	−11.068 ± 0.012
57	44.8 ± 2.7	4.4 ± 0.2	—'—	—'—	1.01 ± 0.03	−11.454 ± 0.007	−11.179 ± 0.007
CNO-overabundance model: $\chi^2_{red} = 1.0457$, d.o.f. $= 199$, $p = 0.31$							
36	4.3 ± 2.3	8.6 ± 0.9	1.0	210 ± 110	1.11 ± 0.06	−11.564 ± 0.012	−11.143 ± 0.012
57	0.6 ± 0.3	4.4 ± 0.2	—'—	—'—	1.01 ± 0.03	−11.454 ± 0.007	−11.221 ± 0.007
XMM-derived abundances model: $\chi^2_{red} = 1.0552$, d.o.f. $= 200$, $p = 0.28$							
36	19.3 ± 1.3	8.6 ± 0.8	0.10	C = 0, O = 29,	1.10 ± 0.06	−11.566 ± 0.012	−11.143 ± 0.012
57	2.6 ± 0.2	4.3 ± 0.2	—'—	N = 345	1.01 ± 0.03	−11.455 ± 0.007	−11.210 ± 0.007
XMM abundances and fixed Galactic column model: $\chi^2_{red} = 1.0547$, d.o.f. $= 200$, $p = 0.28$							
36	19.3 ± 1.3	8.6 ± 0.8	0.10	C = 0, O = 29,	1.11 ± 0.06	−11.566 ± 0.012	−11.141 ± 0.012
57	2.64 ± 0.16	4.3 ± 0.2	—'—	N = 345	1.01 ± 0.03	−11.455 ± 0.007	−11.209 ± 0.007
Two-temperature plasma model: $\chi^2_{red} = 1.0292$, d.o.f. $= 196$, $p = 0.37$							
36	27.6 ± 4.3	6.9 ± 0.7, 0.57 ± 0.07	0.10	C = 0, O = 29,	1.12 ± 0.06	−11.582 ± 0.012	−9.624 ± 0.012
57	3.5 ± 1.5	4.1 ± 0.4, 0.58 ± 0.17	—'—	N = 345	1.01 ± 0.03	−11.456 ± 0.007	−11.074 ± 0.007
Power-law model: $\chi^2_{red} = 1.2667$, d.o.f. $= 200$, $p = 0.006$							
36	24.4 ± 1.8	$\Gamma = 3.30 \pm 0.18$	0.10	C = 0, O = 29,	1.10 ± 0.06	−11.500 ± 0.012	−10.833 ± 0.012
57	4.5 ± 0.2	$\Gamma = 3.92 \pm 0.10$	—'—	N = 345	1.01 ± 0.03	−11.426 ± 0.007	−10.949 ± 0.007

Note. The preferred model is marked in boldface. Column designation: Column 1 – observation time, in units of days since outburst; Column 2 – equivalent hydrogen column density; Column 3 – plasma temperature; Column 4 – abundances of Fe, Co, and Ni (tied together) relative to the solar values; Column 5 – abundances of C, N, and O (tied together for the first two models) relative to the solar values; Column 6 – normalization factor of FPMB relative to FPMA; Column 7 – absorbed model flux in the energy range 3.5–78.0 keV; Column 8 – unabsorbed 3.5–78.0 keV flux.

effective area as a function of energy) calibration files provided by the pipeline are loaded into `XSPEC 12.10.0c` (Arnaud 1996) for further analysis.

To fit the *NuSTAR* observations, we first choose the absorbed optically thin thermal equilibrium plasma model attenuated by photoelectric absorption: `XSPEC` model `constant*vphabs*vapec`. We simultaneously fit all four spectra (FPMA and FPMB spectra obtained at two epochs) allowing for absorbing column (`vphabs`), temperature and normalization factor of `vapec` variations between epochs. The normalization factor between the FPMA and FPMB spectra (represented by the `constant` term) is also allowed to vary between the two epochs. The best-fitting model parameters, together with their estimated 1σ uncertainties, are listed in Table 2.

The observed X-ray spectrum cannot be fit by an absorbed thermal plasma if we assume solar abundances (top left-hand panel of Fig. 1). The χ^2_{red} value we find (3.1; Table 2) corresponds to the null hypothesis probability of $p < <\alpha_{lim}$. The data systematically depart from the model predictions around 6.7 and 20–30 keV, which makes it even less likely to occur by chance compared to the simple χ^2 statistics that does not take into account correlations in residuals (cf. the 'alarm' statistic of Tamuz, Mazeh & North 2006). Throughout this work, we always assume the same abundances for the emitter and absorber (with the exception of Galactic absorbing component that we consider separately below).

At least two variations of the absorbed thermal plasma model are compatible with the observations. The first is a model with Fe abundance (by number) of 0.09 ± 0.03 times the solar value (top right-hand panel of Fig. 1). Fe is present in the nova ejecta (as we clearly see Fe lines in the optical spectrum; Luckas 2018; Aydi et al. 2020), but it may be underabundant with respect to solar values. The second model that provides a good fit to the *NuSTAR* spectrum has solar Fe abundance and overabundance of CNO elements by a factor of 210 ± 110 (bottom left-hand panel of Fig. 1). Novae are known to show overabundance of CNO elements (Williams 1985; Livio & Truran 1994; Gehrz et al. 1998; Schwarz et al. 2001; and the discussion in Section 3.1).

The results in Table 2 do not depend strongly on the specific choice of solar abundances (we used the latest abundances from Asplund et al. 2009 available in `XSPEC`, but also tested the values from Wilms, Allen & McCray 2000 and Lodders 2003). We found that our spectral fits minimally depend on the choice of absorption model, comparing `tbvarabs` (Wilms, Allen & McCray 2000) to `vphabs` (Balucinska-Church & McCammon 1992). We also fit an alternative thermal plasma emission model (`vmekal`; Mewe, Gronenschild & van den Oord 1985; Liedahl, Osterheld & Goldstein 1995), and found the difference with the `vapec` model fit was within the statistical errors. An acceptable fit ($\chi^2_{red} = 1.04$, d.o.f. $= 199$, $p = 0.32$) can be achieved with the simple thermal bremsstrahlung model `bremss` (Kellogg, Baldwin & Koch 1975), implying the absence of obvious emission features in the *NuSTAR* spectra. We prefer the `vapec` model (Brickhouse et al. 2005) over `bremss` as this model is more physically motivated (we expect the line emission to be present at some low level, see Section 2.3).

We also fit the *NuSTAR* spectra with an absorbed thermal plasma model (`vphabs*vapec`), fixing the abundances set to the values derived from our *XMM–Newton* observations described in Section 2.3 and Table 3 (see the bottom right-hand panel of Fig. 1). The C abundance that is not well constrained from the *XMM–Newton* spectroscopy was set to the solar value. We checked that the fit remains essentially the same if we set the C abundance to 0. The

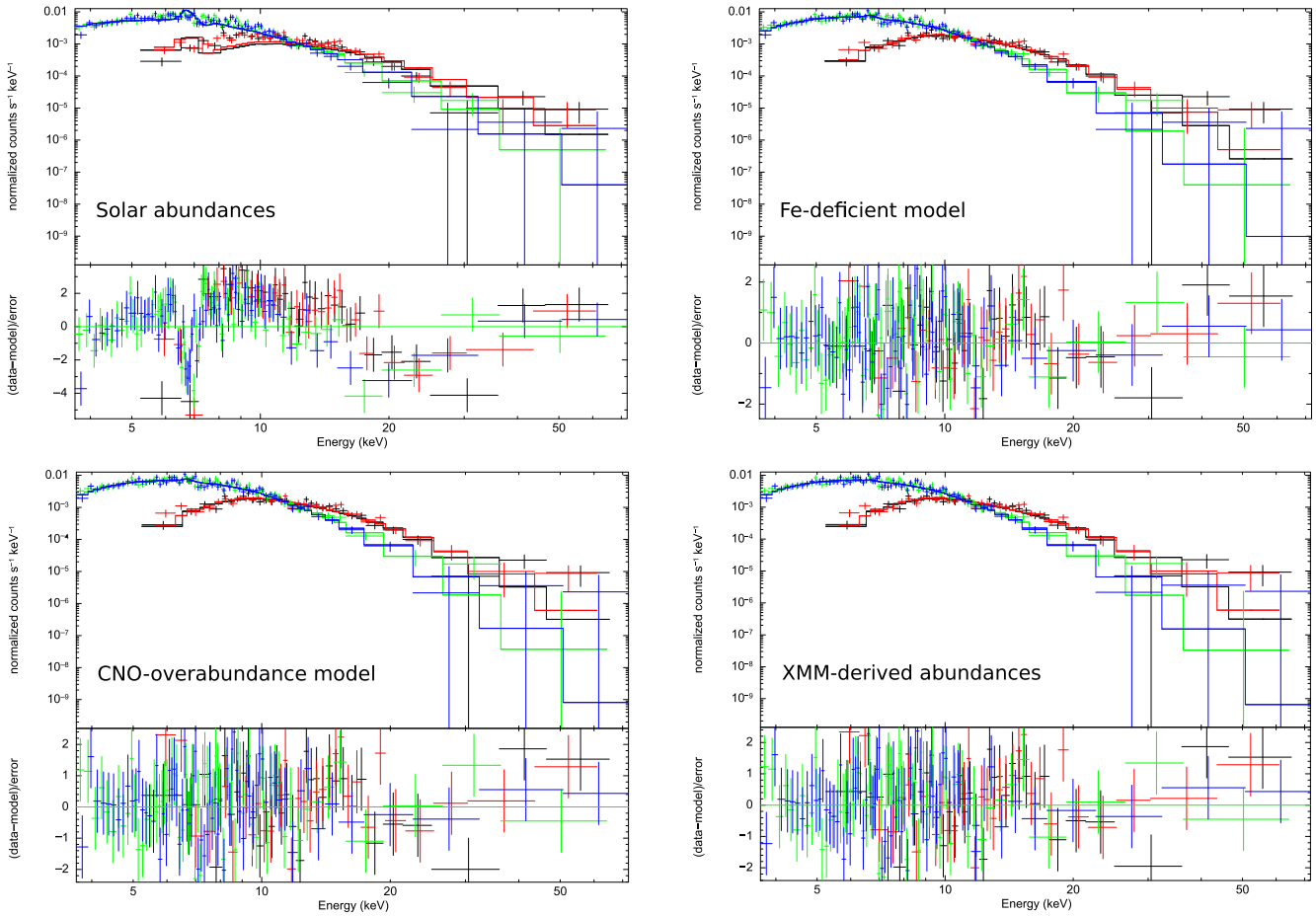

Figure 1. Observed *NuSTAR* spectra compared with four different models for absorbed thermal plasma emission model: abundances fixed to solar (top left-hand panel); FeCoNi abundances tied together and left free to vary (top right-hand panel); CNO abundances tied together and left free to vary, while FeCoNi are fixed to solar values (bottom left-hand panel); and the CNOFeCoNi abundances fixed to the values derived from the *XMM–Newton* observations (bottom right-hand panel; see Table 3). Only the latter three models produce statistically acceptable fits (Table 2). The black and red curves represent spectra obtained with two *NuSTAR* telescopes FPMA and FPMB during the first epoch (t_0 + 36 d), while the green and blue curves are the FPMA and FPMB spectra obtained during the second epoch (t_0 + 57 d).

Co and Ni abundances were set equal to Fe. The resulting plasma temperature (kT) and unabsorbed flux are close to the ones suggested by the CNO-overabundance model, while the absorbing column is best fit by a value intermediate between the CNO-overabundance and Fe-deficient models (Table 2). To estimate the errors in kT and $N_{\rm H}$ resulting from uncertainties in abundances, we vary the N and O abundances within the errors of the *XMM–Newton* spectrum fitting (Table 3), while for Fe we vary the abundances between 0.0 and 0.1 and C in the range 0.0–1.0. These input parameter variations result in best-fitting $N_{\rm H}$ values in the range (15.4–23.5) $\times$ 10^{22} cm^{-2} for the first epoch and (2.1–3.3) $\times$ 10^{22} cm^{-2} for the second epoch (these are full ranges of the obtained best-fitting values, not confidence intervals). The corresponding kT range is 8.63–8.70 keV and 4.32–4.35 keV for the first and second epochs, respectively. Comparing the ranges of kT and $N_{\rm H}$ values obtained with various abundances to the best-fitting values and their uncertainties for the models listed in Table 2, one can see that the temperatures are largely insensitive to the choice of abundances, while the $N_{\rm H}$ values strongly depend on that choice.

As the joint *NuSTAR* and *Swift*/XRT observations of the recurrent nova V745 Sco by Orio et al. (2015) were fit with two-temperature plasma, we tried adding a second `vapec` component to our *NuSTAR* model (`constant*phabs*vphabs*vapec`; Table 2; `phabs` component describes the fixed Galactic $N_{\rm H}$, as discussed below). The fit suggests that a very bright component (0.3–78.0 keV flux of 10^{-7} erg cm^{-2} s^{-1} and 7 $\times$ 10^{-10} erg cm^{-2} s^{-1}, for the first and second epochs, respectively) can be hidden behind the inferred absorbing column, if this second emission component is soft (kT $\simeq$ 0.6 keV). The presence of this low-energy component is not required to obtain a statistically acceptable fit so its flux is highly uncertain and consistent with being zero. The dramatic decrease in the best-fitting flux of this hypothetical low-energy component between the two epochs likely reflects the improving constraints on the soft emission resulting from the decreasing absorbing column, rather than any real change in the emission. The addition of the soft `vapec` component does not change the parameters of the hard `vapec` component; they remain essentially the same as in Table 2 for the single-component emission.

As many novae show supersoft emission at some point in their X-ray evolution (Sections 1.1 and 3.6), we also try to replace the low-energy `vapec` component with a blackbody. This dramatically changes the fit, splitting the flux nearly equally between the `vapec`

Table 3. Parameters of the simultaneous *XMM* (EPIC and RGS) spectra fit with the model `constant*phabs*vphabs*bvapec` plus Gaussian lines (Table 4).

Parameter	Value	Comment
`phabs`		
$N_{\rm H}$ ($\times 10^{21}$ cm^{-2})	$2.4^{+0.4}_{-0.3}$	
`vphabs`		
$N_{\rm H}$ ($\times 10^{21}$ cm^{-2})	$0.12^{+0.03}_{-0.03}$	
`bvapec`		
kT (keV)	$1.07^{+0.04}_{-0.01}$	
Redshift	-2.9×10^{-3}	fixed
Velocity (km s^{-1})	378	fixed
N/N$_\odot$	345^{+93}_{-70}	
O/O$_\odot$	29^{+7}_{-5}	
Ne/Ne$_\odot$	$2.2^{+0.6}_{-0.5}$	
Mg/Mg$_\odot$	$0.6^{+0.2}_{-0.1}$	
Si/Si$_\odot$	$1.1^{+0.2}_{-0.2}$	
Fe/Fe$_\odot$	<0.1	
χ^2_ν	1.15	
d.o.f.	1837	

and `bbody` components. For both epochs, the best-fitting temperature of the blackbody component is >2 keV – so high as to be unphysical for optically thick emission on a white dwarf (SSS are not expected to exceed k$T \approx 0.2$ keV; Wolf et al. 2013).

Spectral fits to *Swift*/XRT observations of V906 Car (Section 2.5) covering a wide time range (Section 2.4) do not require a second emission component and can be described as a single absorbed thermal plasma with temperature and absorbing column that gradually decrease with time. We take this as reassurance that there is no need to artificially introduce a second emission component for fitting the *NuSTAR* observations.

To constrain non-thermal X-rays, we fit the spectrum with an absorbed power-law model `vphabs*pow` (i.e. assuming that *all* X-ray emission is non-thermal – see the discussion in Section 3.4.1). The fit yields values of $\chi^2_{\rm red} = 1.2$, d.o.f. $= 199$, $p = 0.013$ – slightly below our adopted significance level of 0.05. The photon index for the best-fitting power-law model (Table 2) is $\Gamma = 3.9 \pm 0.1$ (Section 3.4.1). The associated absorbing column for the power-law model is higher (by a factor of 1.5 for the XMM abundances model) than for the optically thin plasma model.

Finally, following Nelson et al. (2019), we test the possibility that the *NuSTAR* emission is an (absorbed) combination of an optically thin thermal plasma emission and non-thermal emission represented by a power law (`vapec+pow`). From our absorbed plasma model fits, we see that a power-law component is not required to obtain an acceptable fit to the data; therefore the model flux and photon index are not constrained if both the photon index and normalization factor are left free to vary. To circumvent this, we consider three fixed values of the photon index: $\Gamma = 1.0$, 1.2, and 2.0. In all cases, the contribution of the power-law component is constrained at $\lesssim$2 per cent of the thermal component flux listed in Table 2.

These tested photon index values are the ones expected for the low-energy tail of the GeV emission, as discussed in Section 3.4.1. A different mechanism that may produce non-thermal X-ray emission in novae (which should operate independently of the process responsible for the GeV emission) is the Compton degradation of MeV γ-rays produced by radioactive decay (see Section 1.1; Livio et al. 1992; Suzuki & Shigeyama 2010; Hernanz 2014). Gomez-Gomar et al. (1998) predict flat or inverted (rising) continuum spectra below 100 keV for the Comptonized photons in both CO and ONe novae (which differ by the set of parent radioactive decay lines). As with the low-energy tail of the GeV emission, the observed soft spectrum disfavours Comptonization of the radioactive lines as the source of X-ray emission from V906 Car in the *NuSTAR* band. Nelson et al. (2019) argue that the Compton optical depth in a nova is not sufficient for Compton degradation to produce a detectable hard X-ray flux. In summary, all the expected mechanisms behind non-thermal emission should produce a hard spectrum, while in fact the observed spectrum is soft, consistent with being thermal.

Finally, we construct an '*XMM* abundances and fixed Galactic column' model `constant*phabs*vphabs*vapec` that includes a single emission component (`vapec`) and incorporates our knowledge of the elemental abundances (Section 3.1) and Galactic $N_{\rm H}$ (`phabs`; Section 1.5). We choose this as the preferred model (marked in boldface in Table 2) for the *NuSTAR* spectra of V906 Car.

2.2 *NuSTAR* variability search

We checked for the presence of variability within the two *NuSTAR* observations that lasted 127 and 92 ks wall time (total time including interruptions), respectively (Table 1). The regular interruptions were caused by the Earth occultations of the source. For each of the two observations we generated source and background light curves with `nuproducts` using 5806 s bin size (corresponding to one *NuSTAR* orbital revolution). The background light curve was scaled and subtracted from the source light curve using `lcmath`. We then performed the χ^2 test to determine if the light curves are consistent with the null hypothesis that the source flux does not change during the observation given the errorbars. For a discussion of the χ^2 test in the context of variability search, see de Diego (2010) and Sokolovsky et al. (2017). The test is sensitive to any kind of variability, both periodic and irregular.

We find that the null hypothesis cannot be rejected at the 3σ level, i.e. we found no significant variability within the individual *NuSTAR* observations. The r.m.s. scatter of the *NuSTAR* light curves is 0.008 cts s^{-1} (18 per cent) and 0.007 cts s^{-1} (6 per cent) for the first and the second epoch, respectively. If there is any low-level variability in the source during the times of our observations, the variability amplitude is lower than the above values. Our analysis probes the variability time-scales from ~6 to ~100 ks (variability related to orbital motion of the binary system might be expected on these time-scales). Investigation of variability on a shorter time-scale is limited by S/N, while the upper bound on the detectable variability time-scale is set by the duration of our observations. We leave the search for short time-scale periodic signals (which could be associated with white dwarf rotation) outside the scope of this paper, as we do not expect the X-ray emitting nova shock to be physically tied to the white dwarf surface (for example – its magnetic pole).

2.3 *XMM–Newton* spectroscopy

We requested an *XMM–Newton* target-of-opportunity observation to distinguish between the CNO-overabundant and Fe-deficient models that both fit the *NuSTAR* spectra well, but differ in the predicted $N_{\rm H}$ value by almost two orders of magnitude (Section 2.1). A 51 ks observation (ObsID:0831790401) was conducted on 2018 December 16 (t_0 + 275 d). The observation was only partially (~10–20 per cent of the total effective exposure time) affected by high level of solar particles and all X-ray instruments collected useful data (EPIC cameras: pn,

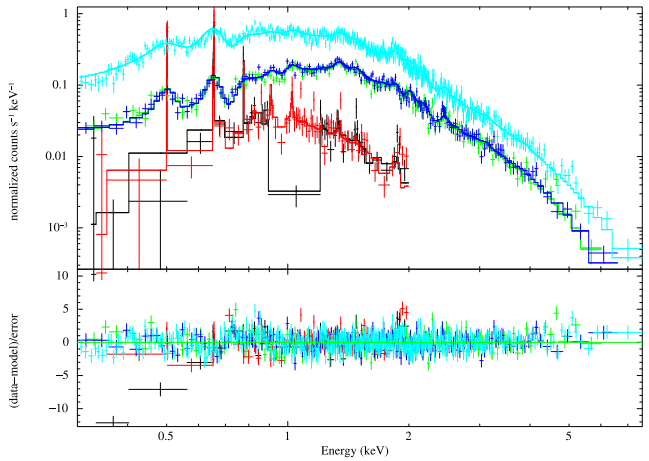

Figure 2. *XMM–Newton* EPIC and (first order) RGS spectra of V906 Car obtained on t_0 + 275. The colour coding is: black – RGS1; red – RGS2; green – EPIC-MOS1; blue – EPIC-MOS2; and cyan – EPIC-pn. The solid lines represent the model described in Table 3.

MOS1, and MOS2; RGS cameras: RGS1 and RGS2). The Optical Monitor had to be blocked due to the presence of the bright star HD 92063 in its field of view, only 2′ from V906 Car (this was the star monitored by BRITE and it also affected the *Swift*/XRT observations; Sections 1.4 and 2.4). The presence of HD 92063 required the use of the thick optical blocking filter with the EPIC cameras. The data analysis was performed through the `XMM-Newton Science Analysis System (SAS) v17.0.0`, using calibration files available in 2018 December. The EPIC data were grouped to have spectra with at least 25 counts per bin for each camera; for the RGS data the value was at least 5 counts per bin. The spectral fit, with `XSPEC 12.9.1m`, assumed the C-Statistic and Chi-Squared for the fit and test statistics, respectively.

The X-rays from V906 Car were clearly detected with all EPIC and RGS instruments (Fig. 2). The average EPIC-pn count rate was 0.810 ± 0.005 cts s^{-1} at the 0.3–8 keV energy range, which corresponds to a total number of background corrected counts of 32 679 for the 40 350 s of the exposure under low level of solar particle contamination. An X-ray source of this brightness should not produce any significant pile-up in any of the *XMM–Newton* instruments and, in fact, there is no evidence of pile-up in the EPIC data from the `sas/epatplot` task.

Table 4. Gaussian lines added to the `bvapec` model.

Lines		Energy (keV)	Wavelength (Å)	Line flux photons (cm^{-2} s^{-1})
Mg XI	r	9.169	1.356	5.2 ± 2.1
	i	9.235	1.346	0
	f	9.314	1.335	$3.5^{+2.1}_{-2.0}$
Ne IX	r	13.447	0.925	0
	i	13.551	0.918	<5.0
	f	13.698	0.908	$14.0^{+2.9}_{-2.8}$
O VII	r	21.602	0.576	8.4 ± 4.0
	i	21.802	0.570	$5.0^{+3.9}_{-3.5}$
	f	22.097	0.563	$16.5^{+4.6}_{-4.5}$
N VI	r	28.792	0.432	$13.9^{+4.8}_{-4.7}$
	i	29.074	0.428	0
	f	29.531	0.421	<9.5

The RGS spectra show a continuum and prominent emission lines, while there is no evidence of absorption lines (Fig. 3). Noticeably, among the emission lines there are the lines of N VII (Kα, analogous to the Lyα line of hydrogen) and O VIII (Kα and Kβ), suggesting a high abundance of these elements.

The EPIC spectra (Fig. 2) do not show the 1 keV 'bump' expected from a number of Fe L-shell lines (analogous to the Balmer series), and there is no sign of the Fe Kα feature – suggesting sub-solar Fe abundance (Section 3.1). The C abundance could not be reliably constrained from the RGS data as the estimate would rely on the C VI Lyα line at 33.7 Å (0.368 keV) in the rest frame, which is located in the noisy part of the spectrum. However, for the solar C/N abundance ratio, the C VI line should be stronger than the detected N VII (24.8 Å, 0.500 keV) line (e.g. Audard et al. 2001) and should have been visible in our RGS spectrum (Fig. 3). The absence of the C VI line, combined with the clear presence of the N VII line imply that the C/N ratio is sub-solar.

The results of a joint fit to EPIC (0.3–8 keV) and RGS (0.65–2 keV) spectra of the absorbed thermal plasma model `phabs*vphabs*bvapec` with the addition of Gaussian lines are presented in Table 3. The adopted abundance table was that of Asplund et al. (2009). The Gaussian lines accounted for excesses that we associate with triplets of resonance (r), intercombination (i), forbidden (f) lines of the He-like ions of Mg XI, Ne IX, O VII, N VI. The fitted line parameters are presented in Table 4. The likely source of the discrepancy between what is predicted by the `bvapec` component

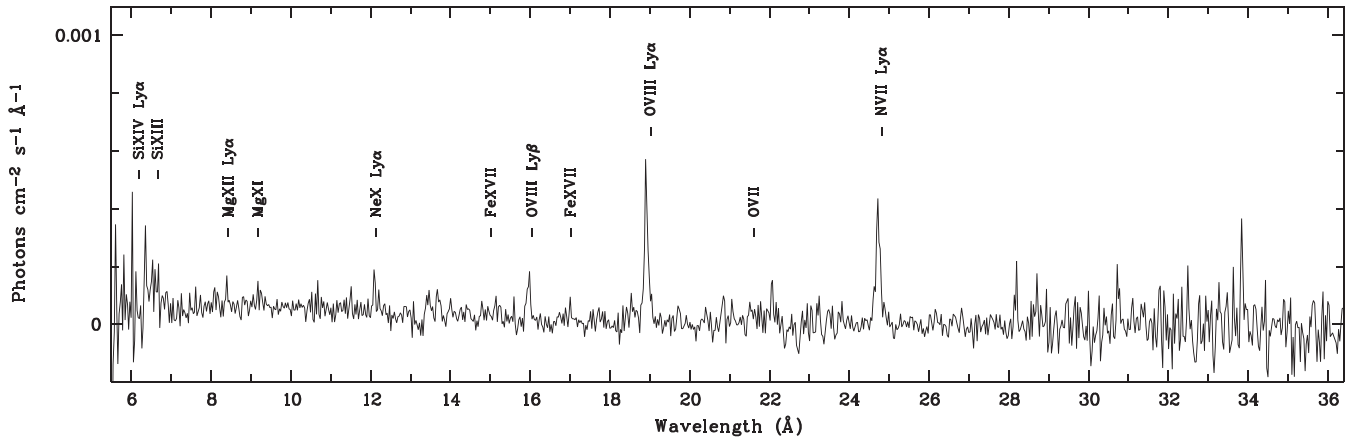

Figure 3. *XMM–Newton* fluxed spectrum of V906 Car combining the first- and second-order spectra from both RGS1 and RGS2.

and what is observed and associated to the triplets is that the single-temperature equilibrium plasma is too crude an approximation of real physical conditions in the nova ejecta that cannot fully describe the grating data.

We use a combination of solar abundances absorber (`phabs`) and variable–abundances absorber (`vphabs`) to account for the Galactic and intrinsic contributions to the total column density, respectively. We let the absorption column parameter for both absorbing components, expressed in the equivalent of hydrogen column ($N_{\rm H}$), to vary freely during the fit. The resulting Galactic $N_{\rm H}$ from X-rays is consistent at the 1σ confidence level with the value estimated from optical extinction (Section 1.5), while the model shows that a non-negligible amount of material is also absorbing X-rays within the nova shell (Table 3).

The emission lines in Fig. 3 appear blueshifted. This indicates that the bulk of the plasma responsible for the emission seen in X-rays is moving towards us. Its radial velocity may be estimated from the redshift parameter of the `bvapec` component in the model. A value of $-870 \pm 60\,{\rm km\,s^{-1}}$ was derived from fitting the same data excluding the energy ranges where the Gaussian lines had to be inserted in the final fit. Then, this value was held fixed for the fit reported in Table 3. Interestingly, had the optical lines been blueshifted by the same velocity, which would have been easily noticeable in spectroscopic observations by Aydi et al. (2020), but no such shift was observed.[5] We do not have a conclusive explanation for this discrepancy, but it seems to be due to opacity and/or asymmetries in the ejecta. One possibility is that the ejecta are opaque to X-rays and we see only the approaching side of the expanding X-ray plasma, while it is fully transparent to photons in the optical by $t_0 + 275$. Alternatively, the X-ray emitting ejecta could be highly asymmetric, with the approaching part emitting much more than the receding part.

A similar blueshift of X-ray emission lines was observed with *Chandra* by Nelson et al. (2008) in the red giant donor recurrent nova RS Oph and by Peretz et al. (2016) in the classical GeV-bright nova V959 Mon. Nelson et al. (2020) confirm the blueshift with *Suzaku* spectroscopy of V959 Mon. The opacity-based explanation of blueshifted emission lines in V959 Mon suggested by Peretz et al. (2016) is similar to that of the blueshifted *absorption* lines observed in the SSS spectra of other novae (Ness 2012). Nelson et al. (2008) speculated that transient highly blueshifted C VI and N VI lines seen in RS Oph may be associated with the asymmetric synchrotron-emitting jet observed with Very Long Baseline Interferometry (VLBI; Rupen, Mioduszewski & Sokoloski 2008).

We use the `bvapec` model instead of `vapec` to account for the velocity- and thermal-broadened emission lines that become important when fitting the grating (RGS) spectra of V906 Car. The line width for the final fit (Table 3) was fixed to the value derived from the preliminary fit that excluded data in the problematic regions where the Gaussian lines had to be added. The line broadening derived from the preliminary fit was $\sigma = 378 \pm 72\,{\rm km\,s^{-1}}$ (Gaussian sigma is the parameter of the `bvapec` model) corresponding to the full width at half-maximum, FWHM $= 2\sqrt{2\ln 2}\sigma = 890\,{\rm km\,s^{-1}}$.

As with the *NuSTAR* spectra (Section 2.1), we tried to add a blackbody emission component to the optically thin thermal plasma model described in Table 3. The resulting blackbody temperature is unphysically high $kT \sim 10$ keV. We interpret it as the absence of any SSS emission during the *XMM–Newton* observation. The optically thin plasma plus blackbody model also does not fit *Swift*/XRT data taken around this time (Section 2.5).

[5]Systemic velocity of $-870 \pm 60\,{\rm km\,s^{-1}}$ would be obvious in the optical spectra collected before the maximum light while the lines are not very broad (the dips of the P Cygni profiles were at $\sim$250 km s^{-1}). On $t_0 + 269$ d, the FWHM of the Balmer lines was $\sim$900 km s^{-1} centred at $50 \pm 100\,{\rm km\,s^{-1}}$ (Aydi et al. 2020).

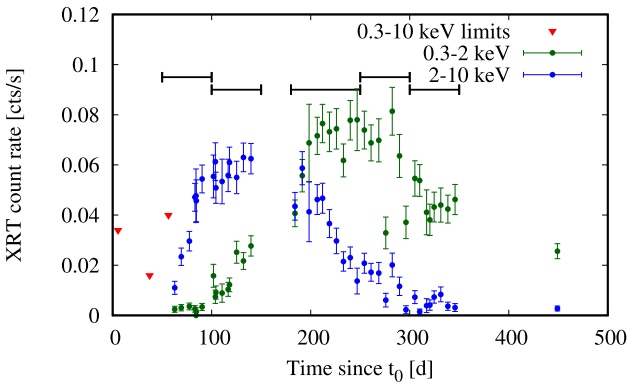

Figure 4. *Swift*/XRT light curve of V906 Car. The red triangles mark the 0.3–10 keV upper limits derived from the Windowed Timing mode observations. The horizontal bars indicate the width of time bins used for the spectral analysis (Table 5).

2.4 *Swift*/XRT monitoring

Swift observed V906 Car on 45 epochs between 2018 March 21 (t_0 + 5.4 d) and 2019 June 8 (t_0 + 449 d). The first three observations on 2018 March 21, April 22, and May 11 resulted in non-detections. The less-sensitive Windowed Timing mode had to be used in the first two observations to reduce optical loading while the nova was still optically bright. During the third observation, the XRT was automatically switching between the Windowed Timing (17 s exposure) and Photon Counting (277 s exposure) modes. V906 Car was clearly detected in the 42 following observations (starting from 2018 May 17, t_0 + 63 d), all performed in the Photon Counting mode with a typical exposure time of 1.5 ks (46.7 ks total exposure). The observations on 2018 September 30 and 2018 November 18 have low signal to noise, as the XRT image of the source was crossed by a bad CCD column reducing the number of detected photons.

We use the standard circular source extraction region with a radius of 20 pix centred at the position derived from Swift/UVOT astrometry (Section 2.6). For the background, we use an annulus centred on the source position with an inner radius of 77 pix and outer radius of 101 pix. This non-standard background extraction region was chosen to avoid the two nearby X-ray sources (clearly visible in the stacked image) and the cluster of optical photons from the nearby bright (V = 5.09) star HD 92063. We use only grade 0 events in the analysis in order to minimize optical loading.

Fig. 4 presents the *Swift*/XRT light curve of V906 Car in the soft (0.3–2 keV) and hard (2–10 keV) bands. The hard flux is steeply rising following the initial detection on 2018 May 11 (t_0 + 63 d), reaches a plateau around 2018 June 14 (t_0 + 90), and then declines after 2018 September 23 (t_0 + 191 d). The soft flux gradually rises from 2018 June 25 (t_0 + 102 d) until 2018 October 8 (t_0 + 207 d), then – after a standstill – it starts to decline on 2018 December 9 (t_0 + 269 d). The peak full band (0.3–10 keV) count rate was reached on 2018 October 14 (t_0 + 212 d) at 0.13 ± 0.01 cts s^{-1}, and is sufficiently low that no pile-up correction is required.

Table 5. Parameters of the *Swift*/XRT spectral models using *XMM*-derived abundances.

Epoch (days)	vphabs $N_{\rm H}$ (10^{22} cm^{-2})	kT (keV)	0.3–10.0 keV Flux $\log_{10}$(erg cm^{-2} s^{-1})	$\chi^2_{\rm red}$	d.o.f.	p
		Model phabs∗vphabs∗vapec				
050–100	0.61 ± 0.12	68 ± 452	−11.155 ± 0.145	0.64	12	0.81
100–150	0.160 ± 0.015	6.2 ± 1.4	−11.148 ± 0.028	0.99	32	0.48
180–250	0.019 ± 0.002	2.18 ± 0.24	−11.288 ± 0.018	1.06	40	0.37
250–300	0.017 ± 0.003	0.98 ± 0.12	−11.705 ± 0.021	1.11	18	0.33
300–350	0.009 ± 0.003	0.74 ± 0.12	−11.916 ± 0.023	1.00	14	0.45
		Model phabs∗vphabs∗bbody				
050–100	0.269 ± 0.080	2.19 ± 0.42	−11.140 ± 0.032	0.42	12	0.96
100–150	0.064 ± 0.012	1.15 ± 0.06	−11.198 ± 0.022	0.82	32	0.76
180–250	0.000 ± 0.001	0.61 ± 0.02	−11.341 ± 0.015	1.19	40	0.19
250–300	0.000 ± 0.003	0.39 ± 0.02	−11.751 ± 0.020	1.83	18	0.02
300–350	0.000 ± 0.001	0.27 ± 0.01	−12.006 ± 0.021	3.33	14	0.00

Note. Column designation: Column 1 – time since outburst; Column 2 – equivalent hydrogen column density; Column 3 – plasma or blackbody temperature; Column 4 – absorbed 0.3–10.0 keV flux; Column 5 – reduced χ^2; Column 6 – number of degrees of freedom; Column 7 – Null hypothesis probability.

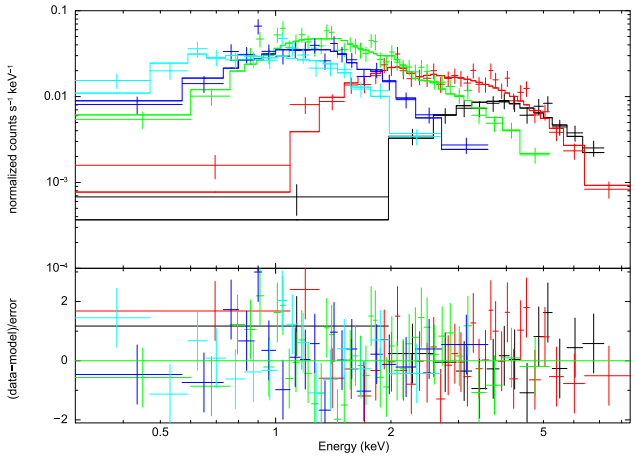

Figure 5. *Swift*/XRT spectra of V906 Car obtained 50–100 (black), 100–150 (red), 180–250 (green), 250–300 (blue), 300–350 (cyan) days after t_0. The solid lines represent phabs∗vphabs∗vapec models described in Table 5.

2.5 *Swift*/XRT spectroscopy

To follow the spectral evolution of V906 Car, we construct five spectra by combining *Swift*/XRT observations taken within ∼50 d intervals marked in Fig. 4 (see Table 5). The spectra are presented in Fig. 5. We binned individual *Swift*/XRT observations to increase the photon statistics (e.g. Nelson et al. 2012), but we note the X-ray spectrum is changing within each bin. This may degrade the quality of the fits reported in Table 5. The bin width of ∼50 d was chosen as a compromise between the photon statistics and the rate of spectral changes.

We fit the data with absorbed thermal plasma models (phabs∗vphabs∗vapec) and absorbed blackbody models (phabs∗vphabs∗bbody), fixing the elemental abundances in the vphabs and vapec components to the values derived from our *XMM–Newton* spectroscopy (Section 2.3; Table 3) and the Galactic absorption phabs (having the solar abundances) to the expected value (Section1.5). The intrinsic absorbing column ($N_{\rm H}$) and plasma/blackbody temperature (kT), as well as the emitting component flux, are left as free parameters. The column densities reported in Tables 2 and 5 refer only to the variable intrinsic vphabs absorption component. The absorbed blackbody fit suggests no intrinsic absorption after t_0 + 150 d, but fails to provide a good fit for the last two Swift spectra (day 250–300 and 300–350). In addition, the blackbody temperatures are unphysically high for an SSS (Wolf et al. 2013). The absorbed optically thin plasma fits all five spectra well, and provide a physically appropriate model for the X-ray emission. The optically thin model is also supported by the *NuSTAR* (Section 2.1) and *XMM–Newton* (Section 2.3) observations. Therefore, we assume that the emission was dominated by the optically thin component at all times.

2.6 *Swift*/UVOT light curve and astrometry

Most of the optical/UV photometry collected with UVOT during the *Swift* monitoring was not useful due to high coincidence losses on the bright source. Only starting from t_0 + 212 d does the source become sufficiently faint to perform photometry in the uvm2 band. The UV light curve shows a smooth decline from uvm2 = 10.44 mag on 2018 October 14 (t_0 + 212 d) to uvm2 = 11.78 mag on 2019 June 8 (t_0 + 449 d). The photometric error is dominated by the uncertainty in the coincidence-loss correction and is expected to be at the level of a few per cent. We used these uvm2 images obtained during the decline phase to measure the astrometric position of V906 Car relative to UCAC3 stars within the UVOT field of view (Zacharias et al. 2010). We measured the nova position with the uncertainty of ∼0.1 arcsec (estimated from the scatter of measurements from multiple images):

10 : 36 : 15.42 − 59 : 35 : 54.0J2000.

2.7 *Fermi*/LAT monitoring

Aydi et al. (2020) performed detailed analysis of *Fermi*/LAT observations of V906 Car, establishing it as the brightest γ-ray emitting nova observed to date, detected during 2018 April 8–30. Unfortunately, the observations were cut short by the failure of the solar panel drive on 2018 March 16 (around t_0) that sent the *Fermi* spacecraft to 'safe mode' with the scientific instruments powered off. The LAT observations resumed on 2018 April 8 (t_0 + 23 d), but were interrupted again for the period 2018 May 1–13 (45–58 d after t_0) by a *Fermi* pointing pattern (needed to keep the stuck solar panel illuminated) that was unfavourable for observations of V906 Car.

Using the power law with exponential cut-off model for the γ-ray spectrum presented in Aydi et al. (2020) and restricting the LAT exposure to the exact time range of the first *NuSTAR* observation (Table 1),

we derive a significant γ-ray detection of V906 Car (test statistic $TS = 283$, or $\sim 17\sigma$ detection; Mattox et al. 1996). Its 100 MeV–300 GeV photon flux is $(1.17 \pm 0.11) \times 10^{-6}$ photons cm^{-2} s^{-1}, and $\nu F_\nu = (1.00 \pm 0.10) \times 10^{-10}$ erg cm^{-2} s^{-1} at photon energy hν = 100 MeV, where h is the Planck constant.

The second *NuSTAR* observation (Table 1) was performed a day before LAT resumed observations of the V906 Car region. So, instead of using strictly simultaneous data, we use the LAT data collected right after the coverage gap, between 2018 May 13 17:01:00 and May 15 04:16 UT (same exposure time as the duration of the first *NuSTAR* observation including interruptions). The LAT observations resulted in a non-detection of V906 Car ($TS = 0$), with an upper limit on the 100 MeV–300 GeV photon flux of $<1.64 \times 10^{-7}$ photons cm^{-2} s^{-1} and $\nu F_\nu < 1.41 \times 10^{-11}$ erg cm^{-2} s^{-1} at hν = 100 MeV.

3 DISCUSSION

3.1 Ejecta abundances

It has long been recognized that nova ejecta are often enriched in heavy elements, compared to the composition of matter accreted from the donor star (e.g. Truran & Livio 1986; Gehrz et al. 1998; Helton et al. 2012). This chemical enrichment is attributed to mixing between the accreted material and the white dwarf itself (Starrfield, Iliadis & Hix 2008). Computer simulations have demonstrated that this mixing probably occurs at the onset of the thermonuclear runaway due to Kelvin–Helmholtz instabilities (Casanova et al. 2011, 2016; Casanova, José & Shore 2018). Thermonuclear burning in the nova event proceeds through the CNO cycle, and may change the relative abundances of C, N, and O, but will not increase the overall abundance of the CNO elements (Starrfield et al. 1972; Truran & Livio 1986). The supersolar N/C ratio found in V906 Car (Section 2.3) demonstrates that the plasma emitting the soft X-ray lines has undergone non-equilibrium CNO burning. The plasma was ejected while in the ^{14}N bottleneck (e.g. Imbriani et al. 2004). Optical spectroscopy often finds in novae an overabundance of nitrogen by two orders of magnitude and oxygen by one order of magnitude compared to solar values, respectively (Gehrz et al. 1998; Arkhipova, Burlak & Esipov 2002; Downen et al. 2013). However, different authors sometimes report quite different abundances for the same nova (for example, compare the abundances for V1974 Cyg reported by Austin et al. 1996; Hayward et al. 1996; Arkhipova, Esipov & Sokol 1997; Vanlandingham et al. 2005); the same is true for the few X-ray derived abundances (e.g. Rauch et al. 2010; Nemeth 2010).

The chemical composition of the nova ejecta is strongly affected by the composition of the white dwarf because we do not generally expect the material accreted from the donor star to have supersolar CNO abundances or to be hydrogen deficient. Therefore, the white dwarf material is being ablated during a nova eruption (e.g. Shara et al. 2018) and we can draw conclusions about the composition of the white dwarf by observing nova ejecta.

Depending on its zero-age main-sequence mass and mass transfer due to binary evolution, the white dwarf hosting nova eruptions may have either a CO or ONe composition. Our *XMM–Newton* spectroscopy of V906 Car implies CNO abundances that are a factor of $\sim$100 supersolar, but near-solar abundance of Ne (Table 3). This suggests that the V906 Car host is a CO white dwarf. The dust formation episode exhibited 50–100 d after outburst is consistent with a CO white dwarf (Aydi et al. 2020), as dust formation is more common in nova ejecta enriched in CO than in ONe (Evans & Rawlings 2008). The CO composition is consistent with a low mass of the white dwarf hinted at by the non-detection of the supersoft emission (Section 3.6). The *XMM–Newton* spectroscopy also suggests sub-solar Fe abundance (Table 3).

3.2 The absence of the Fe Kα feature

We found no evidence of the Fe Kα emission in V906 Car. This is not surprising given that the absence of Fe Kα emission in the X-ray spectra of novae is a long-standing puzzle. At 6.7 keV, this feature probes shock-heated plasma. The two clear examples of novae with no Fe Kα emission are V382 Vel (Section 4.3 in Mukai & Ishida 2001; also no Fe L-shell emission found by Ness et al. 2005) and V959 Mon (Nelson et al. 2020). The weakness of the Fe Kα emission may result from a low abundance of iron in nova ejecta, a high abundance of CNO that would enhance the continuum making the Fe Kα line relatively weaker, or from a non-equilibrium ionization state of the emitting plasma. The Fe II optical spectroscopic type reported for V382 Vel by della Valle, Pasquini & Williams (1999) and Steiner, Campos & Cieslinski (1999) led Mukai & Ishida (2001) to the conclusion that a non-equilibrium ionization state is responsible for the weakness of the iron line. V959 Mon was a neon nova with sub-solar iron abundance (Shore et al. 2013). Novae occurring in symbiotic star systems that include a giant (rather than main sequence) companion to the white dwarf show strong Fe Kα emission (RS Oph and V745 Sco; Nelson et al. 2008; Ness et al. 2009; Orio et al. 2015; Delgado & Hernanz 2019). Such emission was also observed in V2491 Cyg by Takei et al. (2009), Takei et al. (2011), but the nature of the companion star in this system is uncertain. In many cases, the composition of the emitting plasma (rather than its ionization state) determines the strength of the Fe Kα emission.

3.3 Ejecta mass

Observational estimates of how much material is ejected by novae provide a fundamental test of nova models. Ejecta masses, when combined with the Galactic nova rate, constrain the contribution of novae to the chemical evolution of the Galaxy, especially isotopes such as ^{7}Li, ^{13}C, ^{15}N, ^{17}O (Downen et al. 2013; Li et al. 2016; Molaro et al. 2016). The abundances of these isotopes allow laboratory identification of nova dust grains in meteorites (Iliadis et al. 2018).

We can use $N_{\rm H}$ values derived from the X-ray spectral fitting as a function of time after outburst to estimate the ejecta mass. We assume that the source of X-rays is embedded deep into the ejecta, shining through most of it (Section 3.5). The ejecta are modelled as a 'Hubble flow', where the mass is expelled in a single impulse and is uniformly distributed over a range of velocities spanning from $v_{\rm min}$ to $v_{\rm max}$. This corresponds to the mass density $\propto r^{-2}$ (e.g. Seaquist & Bode 2008). For $v_{\rm max}$, we take the maximum expansion velocity measured from the wavelength difference between the absorption dip and the emission peak of the P Cygni profiles of Balmer lines, 2500 ± 100 km s^{-1} (measured around $t_0 + 24$ d; Aydi et al. 2020, Harvey et al., in preparation). In the Hubble flow model the slower moving ejecta will dominate the $N_{\rm H}$ at later epochs, when the faster moving ejecta have dispersed; the total ejecta mass in this model critically depends on the choice of $v_{\rm min}$. Following Chomiuk et al. (2014b), we assume $v_{\rm min} = 0.2 v_{\rm max}$ that is in the middle of the range of values reported in the literature from modelling the multifrequency radio light curves of novae (Seaquist & Bode 2008; Weston et al. 2016a,b; Finzell et al. 2018); see Appendix A.

We apply the Hubble flow model to the $N_{\rm H}$ evolution derived from the *NuSTAR* spectra fitted with the preferred model (Fig. 6). Assuming that the ejecta began expanding at t_0, there is no acceptable

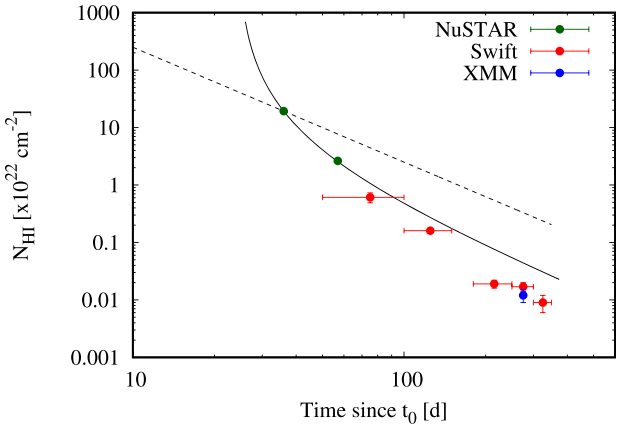

Figure 6. The evolution of the absorbing column intrinsic to V906 Car as a function of time. The solid curve represents the delayed ejection model fitting *NuSTAR* observations. The dashed line represents the model with prompt ejection at t_0, which predicts the same column density on $t_0 + 36$ as the delayed ejection model.

fit to the $N_{\rm H}$ evolution (see the dashed line in Fig. 6). A good fit can be achieved if we assume that the mass was ejected at $t_0 + 24$ d (the solid curve in Fig. 6). Other novae have shown evidence for ejection of mass delayed weeks to months after the start of outburst: V2362 Cyg (Kimeswenger et al. 2008; Lynch et al. 2008; Arai et al. 2010), T Pyx (Nelson et al. 2014; Chomiuk et al. 2014b) and V959 Mon (Chomiuk et al. 2014a; Linford et al. 2015; Nelson et al. 2020). In this model, the ejecta mass is $2.8 \times 10^{-5}\,{\rm M}_\odot$ assuming spherical symmetry and the range of expansion velocities between $v_{\rm max} = 2500\,{\rm km\,s^{-1}}$ and $v_{\rm min} = 0.2 v_{\rm max}$. The ejecta mass estimate strongly depends on these assumptions. Setting $v_{\rm max} = 600\,{\rm km\,s^{-1}}$ (the slow component observed by Aydi et al. 2020) would decrease the ejecta mass estimate by a factor of 20. Setting $v_{\rm min} = 0.1 v_{\rm max}$ would increase the mass estimate by a factor of 4. In the above ejecta mass calculation we counted only the hydrogen atoms. The hydrogen mass should be multiplied by a factor of 1.90 for the derived nova abundances (Table 3; the factor would be 1.36 for the solar abundances of Asplund et al. 2009).

Taking into account the chemical composition of the ejecta and setting $v_{\rm min} \ll 0.2 v_{\rm max}$ is needed to reconcile the above X-ray absorption-based ejecta mass estimate with the lower limit of $2 \times 10^{-4}\,{\rm M}_\odot$ derived from radio observations of V906 Car by Aydi et al. (2020) and the optical spectroscopy-based estimate of $6 \times 10^{-4}\,{\rm M}_\odot$ by Pavana et al. (2020). Alternatively, the discrepancy may be attributed to the X-ray-emitting region being located above a considerable part of the ejecta (Section 3.5) or ejecta being asymmetric (our line of sight may have less-than-average amount of X-ray absorbing material). Ejecta mass estimates from the radio light curve and optical spectroscopy are also subject to their own model assumptions (such as clumpiness and temperature distribution).

Our conclusion about the delayed ejection depends on the assumption of a one-time ejection with a range of velocities. Other scenarios may not require the delayed ejection and imply substantially different ejecta mass given the same observed $N_{\rm H}$. The mass may be continuously ejected over an extended period of time. The ejecta may experience (a period of) continuous acceleration (e.g. slow circumbinary material gradually pushed away by the fast white dwarf wind). The ejecta may be asymmetric. The observation that $N_{\rm H}$ values measured with *Swift* and *XMM–Newton* up to $t_0 + 350$ d generally follow the trend predicted by the delayed one-time ejection model fitting *NuSTAR* observations on $t_0 + 36$ d and $t_0 + 57$ d (Fig. 6) suggests that this simple model may be a reasonable approximation of the actual ejection.

Table 6. X-ray to γ-ray monochromatic flux ratio in νF_ν units.

Nova	$L_{20\,{\rm keV}}/L_{100\,{\rm MeV}}$	Reference
V339 Del	$<4.0 \times 10^{-3}$	Vurm & Metzger (2018)
V5668 Sgr	$<1.7 \times 10^{-3}$	Vurm & Metzger (2018)
V5855 Sgr	0.01	Nelson et al. (2019)
V906 Car	0.02	this work

3.4 The L_X/L_γ ratio

The ratio between the X-ray luminosity, L_X, and γ-ray luminosity, L_γ, provides insights into the physics of shocks in novae.

3.4.1 Non-thermal X-rays

Vurm & Metzger (2018) discuss the possibility of non-thermal X-rays in novae, predicting the spectral slope $\nu F_\nu \propto \nu^{0.8}$ ($\Gamma = 1.2$; Section 1.6) in the hard X-ray band ($\gtrsim$10 keV). The observed *NuSTAR* spectrum of V906 Car is very soft, having $\Gamma > 2$ when fit with a single power-law (Section 2.1). This supports the interpretation that the observed X-ray emission is thermal, rather than non-thermal. Another key prediction of Vurm & Metzger (2018) is the existence of a lower limit on the ratio of non-thermal X-ray to γ-ray fluxes. In νF_ν units the limits are $L_X/L_\gamma > 10^{-3}$ for a leptonic origin of γ-rays, and $L_X/L_\gamma > 10^{-4}$ for the hadronic model.

Table 6 summarizes the available $L_{20\,{\rm keV}}/L_{100\,{\rm MeV}}$ measurements. *NuSTAR* observations of novae V339 Del and V5668 Sgr, carried out during the GeV-bright phase, yielded non-detections in the hard X-ray band (Mukai et al., in preparation). Vurm & Metzger (2018) used these upper limits on the L_X/L_γ ratio to suggest that the hadronic rather than leptonic mechanism is responsible for the γ-ray emission of novae. Nelson et al. (2019) observed the nova V5855 Sgr with *NuSTAR* 12 d after eruption, while it was still detected in γ-rays by *Fermi*/LAT. V5855 Sgr is the first nova in which >10 keV X-rays and γ-rays were detected simultaneously. The *NuSTAR* spectrum of V5855 Sgr is mostly featureless and can be fit by either an absorbed bremsstrahlung (all emission in *NuSTAR* band is thermal) or an absorbed power law (all emission is nonthermal) model. Nelson et al. (2019) prefer the thermal emission model by invoking the spectral slope argument (that low-energy tail of GeV emission should result in a hard *NuSTAR* spectrum while the best-fitting power law has $\Gamma = 3.6^{+1.3}_{-1.0}$). Therefore, the $L_{20\,{\rm keV}}/L_{100\,{\rm MeV}}$ ratio measured by Nelson et al. (2019) is considered by the authors an upper limit on any non-thermal emission (Table 6). This upper limit in V5855 Sgr is consistent with both the leptonic and hadronic scenarios (Vurm & Metzger 2018).

3.4.2 Thermal X-rays

Thermonuclear reactions heat the white dwarf atmosphere, but only to temperatures <0.2 keV (Wolf et al. 2013), which is identified with supersoft X-ray emission (Section 1.1). Thermal emission of novae with $kT \gtrsim 0.5$ keV is attributed to optically thin shock-heated plasma. The Rankine–Hugoniot conditions for a strong shock propagating in monoatomic gas (with polytropic exponent 5/3) relate the post-shock

temperature ($T_{\rm shock}$) to the shock velocity ($v_{\rm shock}$):

$$kT_{\rm shock} = \frac{3}{16}\mu m_{\rm p} v_{\rm shock}^2 \quad (2)$$

(equation 30 of Metzger et al. 2014), where $m_{\rm p}$ is the proton mass, k is the Boltzmann constant, μ is the mean molecular weight. For the fully ionized gas with the solar abundances as derived by Asplund et al. (2009), $\mu = 0.60$. Meanwhile, $\mu = 0.74$ for the nova abundances from Table 3. From equation (2), we conclude that $v_{\rm shock}$ decreased from 2400 to 1700 km s^{-1} between the two *NuSTAR* epochs (Table 2). The shock velocity of 2400 km s^{-1} observed on day 36 is consistent with the velocity of the fastest wind, which starts around day 23 and remains visible in the optical line profile until at least day 35 (Aydi et al. 2020). The hypothetical second emitting component with kT = 0.6 keV considered in the two temperature plasma model described in Section 2.1 would correspond to $v_{\rm shock} = 640$ km s^{-1}. We point out that $v_{\rm shock}$ is different from the ejecta expansion velocity, unless the ejecta slam into pre-existing low-velocity material. If the shock is formed at the interface between the slow and fast wind, $v_{\rm shock}$ would correspond to the velocity difference between the two components.

Radiative shocks should produce thermal X-ray emission that is at least 1–2 orders of magnitude brighter (in νF_ν units) than the GeV emission of the non-thermal particles (Metzger et al. 2015). This is in sharp contrast with our *NuSTAR* observations, which show that the X-ray emission is almost two orders of magnitude fainter than the *Fermi*/LAT emission: $L_{20\,\rm keV}/L_{100\,\rm MeV} = 0.02$ (Section 3.4.1). A similar discrepancy is reported by Nelson et al. (2019) for V5855 Sgr and even stronger ones are implied by the non-detections of V339 Del and V5668 Sgr (table 6; Mukai et al., in preparation). Thermal X-rays from the radiative shock can be suppressed because of a corrugated shock front geometry (Steinberg & Metzger 2018) or by redistributing emission because of Compton scattering in a highly non-spherical nova ejecta (Nelson et al. 2019). Each of the two effects can suppress the X-ray emission by an order of magnitude, which is still not sufficient to account for the 3–4 orders of magnitude difference between the predictions (Metzger et al. 2015) and observations (Table 6).

The inferred properties of the shock producing the observed thermal X-rays are inconsistent with the inferred properties of the shock accelerating the GeV γ-ray emitting particles. Earlier, Vlasov, Vurm & Metzger (2016) suggested the presence of different shock systems responsible for the thermal X-ray and non-thermal radio emission in novae. The correlated optical and GeV variability seen in two novae by Li et al. (2017) and Aydi et al. (2020), together with GeV-to-optical flux ratios ≈0.01, imply that the majority of GeV-emitting shock energy eventually emerges as radiation. The shock should produce most of its thermal output in X-rays that get absorbed and eventually escape as optical photons (see Section 3.1 in Metzger et al. 2014). X-rays from the GeV-emitting shock may be completely hidden from our *NuSTAR* observations if the emission is sufficiently soft (k$T \lesssim 0.6$ keV corresponding to $v_{\rm shock} = 640$ km s^{-1}) and if it disappears before *Swift* observations can probe these low energies (because of decreasing intrinsic absorption), after $t_0 + 63$ d.

3.5 Location of the X-ray-emitting shock

The location of the X-ray emitting shock with respect to the binary system, the expanding nova ejecta and the γ-ray emitting shock is unclear. Here, we discuss a few possibilities.

Metzger et al. (2014) consider the collision of nova ejecta with a dense external shell and suggest the forward shock as the source of X-rays. There is no widely accepted observational evidence for the existence of dense circumbinary material in classical nova systems (with a dwarf donor; Harrison et al. 2013a; Hoard et al. 2014, but see McLoughlin et al. 2020), however, such material clearly exists in symbiotic systems (with giant donors; e.g. Seaquist & Taylor 1990).

Optical spectroscopy has long indicated that, in many cases, nova outbursts produce multiple ejections with different velocities (e.g. McLaughlin 1944; Friedjung 1966, 2011; Aydi et al. 2019). Aydi et al. (in preparation) argue that the presence of at least two physically distinct outflows is a common feature of novae. Collision between a high-velocity wind that catches up with a low-velocity ejection launched earlier may produce the shock. A specific variation on the multiple outflows scenario was proposed by Chomiuk et al. (2014a) based on radio imaging of the γ-ray-detected nova V959 Mon. In this scenario, a slow equatorial outflow is launched at the time of the nova outburst, and is later followed by a fast wind driven by the intense radiation from the white dwarf. The slow outflow is drawn from the puffed-up nova envelope that may remain gravitationally bound to the system, and gradually expands due to energy input from the binary system's orbital motion (Pejcha, Metzger & Tomida 2016), in analogy to the common envelope phase in binary system evolution (Livio et al. 1990; Ivanova et al. 2013). The shocks in this scenario form at the interface between the white dwarf wind and the equatorial outflow.

One could also imagine that the accretion disc around a white dwarf could survive the nova explosion. The presence of accretion discs was reported in novae during the SSS phase (Sala et al. 2010; Walter & Battisti 2011; Mason & Walter 2014; Aydi et al. 2018). The shock may form at the interface between the white dwarf wind and the accretion disc. The orbital motion of the donor star within the expanded atmosphere of the nuclear-burning white dwarf may create a bow shock. The expected orbital velocity ∼200 km s^{-1} is smaller than the shock velocity derived from the plasma temperature (equation 2), and it should not decrease with time (Section 3.4.2).

Finally, it has been well established that radiation-driven winds of massive stars are clumpy (Martínez-Núñez et al. 2017; Sundqvist, Owocki & Puls 2018). Interaction of the dense clumps with the surrounding low-density wind and with each other produce strong shocks (Owocki, Castor & Rybicki 1988; Feldmeier, Puls & Pauldrach 1997). A hot nuclear-burning white dwarf should drive an intense wind. The combination of bound-free and line opacities is driving the wind of hot massive stars, while in the even hotter novae the dominating opacity mechanism should be Thomson scattering (Shaviv 2001a). At super-Eddington luminosities found in novae, the Thomson scattering-supported wind should be inhomogeneous, as it originates in an unstable atmosphere (Shaviv 2001b). Indeed, the ejecta of novae are well known to be clumpy, as demonstrated by resolved imaging (O'Brien & Bode 2008) and spectroscopic observations (e.g. Williams 1994; Shore et al. 2013; Mason et al. 2018). Multiple shocks associated with multiple clumps distributed across the ejecta may give rise to nova X-ray emission (Williams 2016) – but in this case we might expect shocks at a range of absorbing columns, including some that are relatively unabsorbed even at early times. Nelson et al. (2008) consider this scenario for the X-ray emission of RS Oph with the shocked clumps originating either in the nova ejecta or in the red giant companion wind (red giant winds are reported to be clumpy; Crowley 2006; Espey & Crowley 2008; with maser observations indicating volume filling factors <0.01; Richards et al. 2012).

As we have an estimate of the shock velocity (Section 3.4.2), the X-ray variability time-scale, $t_{\rm var}$, can give us a clue about the size of the X-ray emitting region, $l = v_{\rm shock} t_{\rm var}$. The absence of variability on a ∼100 ks time-scale (Section 2.2) suggests that on day 36 the

X-ray-emitting region was $\gtrsim$1 au in size. Alternatively, the emitting region(s) might be small, but produce a stable flux of X-rays, or variations from a large number of emitting regions might average out (Feldmeier, Puls & Pauldrach 1997).

3.6 The missing SSS phase

A notable feature of V906 Car is the absence of a pronounced boundary between hard and supersoft X-ray emission observed in many other novae (Schwarz et al. 2011; Ness 2012; Page et al. 2013; Page, Beardmore & Osborne 2019). This is apparent from both the spectral fits (Table 5, Fig. 5) and from the absence of an abrupt increase in soft X-rays in Fig. 4. Instead, the soft X-rays gradually brighten as the hard X-rays gradually fade.

The duration, temperature, and luminosity of the SSS emission depend on the mass of the white dwarf. Higher mass white dwarfs tend to produce brighter, hotter, and more short-lived SSS compared to their low-mass counterparts (Henze et al. 2011; Wolf et al. 2013; Wolf 2017). The absence of SSS emission in V906 Car suggests that it either ended before the nova ejecta became transparent to soft X-rays (a short-lived SSS implies a high mass of the white dwarf) or that the SSS emission was sufficiently faint and soft to be completely hidden by the Galactic absorption (Section 1.5) implying a low-mass white dwarf. The support the latter possibility comes from the CO composition of the white dwarf (Section 3.1) together with the slow decline of the nova (Yaron et al. 2005; Shara et al. 2017) and the slow ejecta velocities observed from the optical spectral lines (Kovetz & Prialnik 1985; Friedjung 1992; Kato & Hachisu 1994), which are associated with a low-mass white dwarf.

Another speculative possibility is that the shock-heated region may be so close to the white dwarf (i.e. the surviving accretion disc scenario in Section 3.5) that shock energy may contribute to heating the outer layers of the white dwarf. In this scenario, shocks and nuclear burning heat essentially the same region of plasma near the surface of the white dwarf, blurring the boundary between the shock-powered and SSS emission. The blackbody fits to the *Swift*/XRT spectra after $t_0 + 250$ d result in $kT < 0.5$ keV (Table 5), i.e. qualifying as SSS emission (according to an observational definition; Sections 1.1 and 3.4.2), but are still considerably hotter than the emission expected even from a very massive white dwarf (Wolf et al. 2013).

4 CONCLUSIONS

We conducted a joint analysis of *NuSTAR*, *XMM–Newton*, *Swift*, and *Fermi*/LAT observations of nova V906 Car. The observation 36 d after the explosion was only the second simultaneous *NuSTAR*/*Fermi* detection (out of four classical novae observed – Table 6). Our conclusions can be summarized as follows:

(i) The X-ray emission of V906 Car in the *NuSTAR* band is soft (the photon index would be $\Gamma \simeq 4$; Section 2.1), and we attribute it to optically thin thermal plasma of temperature $kT = 4$–9 keV (Table 2). We found no evidence for a non-thermal contribution to the 3.5–78 keV emission (Section 3.4.1).

(ii) The nova ejecta have highly non-solar abundances, consistent with ejection from the surface of a CO white dwarf (Section 3.1).

(iii) V906 Car does not show distinct SSS emission, which may be an indication of a low-mass white dwarf (Section 3.6). Instead, the X-ray spectral evolution of V906 Car can be described as a single optically thin thermal emission component of gradually decreasing temperature hidden behind a column density that is also decreasing with time (Section 2.5).

(iv) The evolution of the absorbing column $N_{\rm H}$ with time (Fig. 6) implies that 5×10^{-5} M$_\odot$ (corrected for heavy element abundances; Section 3.3) were ejected 24 d after the start of the eruption. Gradual acceleration of the ejecta and ejection over a prolonged period of time are the alternative to the late ejection scenario.

(v) The absence of variability on $\lesssim$100 ks time-scale in the *NuSTAR* band suggests that the X-ray emitting region is larger than $\sim$1 au (Section 3.5).

(vi) Contrary to theoretical expectations, the *thermal* hard X-ray emission observed by *NuSTAR* is much fainter (in νF_ν units) than the simultaneous GeV γ-ray emission ($L_{20\,\rm keV}/L_{100\,\rm MeV} = 0.02$; Section 3.4). V906 Car is the fourth γ-ray emitting nova to demonstrate such low L_X/L_γ (Table 6). The low X-ray luminosity may indicate that the shocks responsible for the X-ray emission are not the same as the ones accelerating GeV-emitting particles, that X-rays are suppressed in nova radiative shocks, that particle acceleration is surprising efficient, and/or that the radiative shock approximation is not applicable to these shocks (Section 3.4.2).

(vii) The *non-thermal* hard X-ray emission contribution is constrained at $L_{20\,\rm keV}/L_{100\,\rm MeV} < 5 \times 10^{-4}$. This rules out leptonic models of the nova GeV emission (Section 3.4.1).

Future VLBI radio observations may image synchrotron emission of the accelerated particles and pinpoint the location and geometry of γ-ray and X-ray emitting shocks (however, free–free absorption and synchrotron self-absorption may hamper early radio imaging). Simultaneous GeV and hard X-ray observations of future novae may provide further insights into the 'missing X-rays' problem (both thermal and non-thermal). The ultimate proof for hadronic mechanism of the GeV emission will be detection of neutrino emission from a nova.

ACKNOWLEDGEMENTS

KVS thanks Dr. Victoria Grinberg for drawing attention to the problem of clumpy stellar winds and Dr. Marina Orio for pointing out the report of possible X-ray fireball detection. We thank the anonymous referee for the very useful comments. This material is based upon work supported by the National Science Foundation under grant AST-1751874. We acknowledge support for this work from NASA grants Fermi/80NSSC18K1746 and NuSTAR/80NSSC19K0522 and from a Cottrell Scholarship from the Research Corporation. KLP acknowledges support from the UK Space Agency. JS acknowledges support from the David & Lucile Packard Foundation. KLL is supported by the Ministry of Science and Technology of the Republic of China (Taiwan) through grant 108-2112-M-007-025-MY3. IV acknowledges support by the Estonian Research Council grants IUT26-2 and IUT40-2, and by the European Regional Development Fund (TK133).

DATA AVAILABILITY

The processed data underlying this work are available at the request to the first author and here.[6] The raw data are publicly available at *NuSTAR*, *XMM–Newton*, *Swift*, and *Fermi* science archives.

REFERENCES

Abdo A. A. et al., 2009, Astropart. Phys., 32, 193
Abdo A. A. et al., 2010, Science, 329, 817

[6] http://scan.sai.msu.ru/~kirx/data/V906_Car_public_data/

Ackermann M. et al., 2012, ApJS, 203, 4
Ackermann M. et al., 2014, Science, 345, 554
Arai A. et al., 2010, PASJ, 62, 1103
Arkhipova V. P., Burlak M. A., Esipov V. F., 2002, Astron. Lett., 28, 100
Arkhipova V. P., Esipov V. F., Sokol G. V., 1997, Astron. Lett., 23, 713
Arnaud K., Smith R., Siemiginowska A., 2011, Handbook of X-ray Astronomy. Cambridge University Press, Cambridge, UK
Arnaud K. A., 1996, in Jacoby G. H., Barnes J., eds, ASP Conf. Ser. Vol. 101, Astronomical Data Analysis Software and Systems V. Astron. Soc. Pac., San Fransisco, p. 17
Asplund M., Grevesse N., Sauval A. J., Scott P., 2009, ARA&A, 47, 481
Atwood W. B. et al., 2009, ApJ, 697, 1071
Audard M., Behar E., Güdel M., Raassen A. J. J., Porquet D., Mewe R., Foley C. R., Bromage G. E., 2001, A&A, 365, L329
Austin S. J., Wagner R. M., Starrfield S., Shore S. N., Sonneborn G., Bertram R., 1996, AJ, 111, 869
Aydi E. et al., 2018, MNRAS, 480, 572
Aydi E. et al., 2019, preprint (arXiv:1903.09232)
Aydi E. et al., 2020, Nat. Astron.
Bailer-Jones C. A. L., Rybizki J., Fouesneau M., Mantelet G., Andrae R., 2018, AJ, 156, 58
Bajaja E., Arnal E. M., Larrarte J. J., Morras R., Pöppel W. G. L., Kalberla P. M. W., 2005, A&A, 440, 767
Balucinska-Church M., McCammon D., 1992, ApJ, 400, 699
Barthelmy S. D. et al., 2005, Space Sci. Rev., 120, 143
Blandford R. D., 1994, ApJS, 90, 515
Bode M. F., Evans A., 2008, Cambridge Astrophysics Series, No. 43. Cambridge University Press, Cambridge
Boettcher M., 2010, preprint (arXiv:1006.5048)
Brickhouse N. S., Desai P., Hoogerwerf R., Liedahl D. A., Smith R. K., 2005, in Smith R., ed., AIP Conf. Proc. Vol. 774, X-ray Diagnostics of Astrophysical Plasmas: Theory, Experiment, and Observation. Am. Inst. Phys., New York, p. 405
Burrows D. N. et al., 2005, Space Sci. Rev., 120, 165
Caprioli D., Spitkovsky A., 2014, ApJ, 783, 91
Casanova J., José J., García-Berro E., Shore S. N., 2016, A&A, 595, A28
Casanova J., José J., García-Berro E., Shore S. N., Calder A. C., 2011, Nature, 478, 490
Casanova J., José J., Shore S. N., 2018, A&A, 619, A121
Chang J. et al., 2017, Astropart. Phys., 95, 6
Chen B.-Q. et al., 2019, MNRAS, 483, 4277
Cheung C. C. et al., 2016, ApJ, 826, 142
Chomiuk L. et al., 2014a, Nature, 514, 339
Chomiuk L. et al., 2014b, ApJ, 788, 130
Corbett H., Law N., Goeke E., Ratzloff J., Howard W., Fors O., del Ser D., Quimby R. M., 2018, Astron. Telegram, 11467, 1
Crowley C., 2006, PhD thesis, Trinity College Dublin
de Diego J. A., 2010, AJ, 139, 1269
Delgado L., Hernanz M., 2019, MNRAS, 490, 3691
Della Valle M., Izzo L., 2020, A&AR, 28, 3
della Valle M., Pasquini L., Williams R., 1999, IAU Circ., No. 7193
den Herder J. W. et al., 2001, A&A, 365, L7
Domingo A., Hernanz M., Kuulkers E., Kuin P., 2018, Astron. Telegram, 11677, 1
Downen L. N., Iliadis C., José J., Starrfield S., 2013, ApJ, 762, 105
Drake J. J., Starrfield S., Osborne J.-U. N. J. P., Page K., Shore S. N., Wagner R. M., Woodward C. E., 2014, Astron. Telegram, No. 5920
Espey B. R., Crowley C., 2008, Mass-loss from Red Giants, ASPC vol.401, p. 166
Evans E., Rawlings J. M. C., 2008, in Bode M. F., Evans A., eds, Cambridge Astrophysics Series, No. 43, Cambridge University Press, Cambridge, p. 308
Feldmeier A., Puls J., Pauldrach A. W. A., 1997, A&A, 322, 878
Finzell T. et al., 2018, ApJ, 852, 108
Franckowiak A., Jean P., Wood M., Cheung C. C., Buson S., 2018, A&A, 609, A120
Friedjung M., 1966, MNRAS, 132, 317
Friedjung M., 1992, A&A, 262, 487
Friedjung M., 2011, A&A, 536, A97
Friedman S. D. et al., 2011, ApJ, 727, 33
Gehrels N., 1997, Nuovo Cimento B, 112B, 11
Gehrels N. et al., 2004, ApJ, 611, 1005
Gehrz R. D., Truran J. W., Williams R. E., Starrfield S., 1998, PASP, 110, 3
Ghisellini G., 2013, Lecture Notes in Physics, Vol. 873. Springer International Publishing Switzerland
Gomez-Gomar J., Hernanz M., Jose J., Isern J., 1998, MNRAS, 296, 913
Güver T., Özel F., 2009, MNRAS, 400, 2050
Hachisu I., Kato M., 2014, ApJ, 785, 97
Harrison F. A. et al., 2013b, ApJ, 770, 103
Harrison T. E., Hamilton R. T., Tappert C., Hoffman D. I., Campbell R. K., 2013a, AJ, 145, 19
Hartmann L., Kenyon S. J., 1996, ARA&A, 34, 207
Hasinger G., 1994, Rev. Mod. Astron., 7, 129
Hayward T. L. et al., 1996, ApJ, 469, 854
Helton L. A. et al., 2012, ApJ, 755, 37
Henze M. et al., 2011, A&A, 533, A52
Henze M. et al., 2014, A&A, 563, A2
Hernanz M., 2014, in Woudt P. A., Ribeiro V. A. R. M., eds, ASP Conf. Ser. Vol. 490, Stellar Novae: Past and Future Decades. Astron. Soc. Pac., San Fransisco, p. 319
Hernanz M., José J., 2006, New Astron. Rev., 50, 504
Hernanz M., Sala G., 2005, in Hameury J. M., Lasota J. P., eds, ASP Conf. Ser. Vol. 330, The Astrophysics of Cataclysmic Variables and Related Objects. Astron. Soc. Pac., San Fransisco, p. 447
Hernanz M., Sala G., 2010, Astron. Nachr., 331, 169
Hernanz M. et al., 2002, in Hernanz M., José J., eds, AIP Conf. Ser. Vol. 637, Classical Nova Explosions. Am. Inst. Phys., New York, p. 435
Heywood I., O'Brien T. J., Eyres S. P. S., Bode M. F., Davis R. J., 2005, MNRAS, 362, 469
Hjellming R. M., 1996, in Taylor A. R., Paredes J. M., eds, ASP Conf. Ser. Vol. 93, Radio Emission from the Stars and the Sun. Astron. Soc. Pac., San Fransisco, p. 174
Hjellming R. M., Wade C. M., Vandenberg N. R., Newell R. T., 1979, AJ, 84, 1619
Hoard D. W. et al., 2014, ApJ, 786, 68
Iliadis C., Downen L. N., José J., Nittler L. R., Starrfield S., 2018, ApJ, 855, 76
Imbriani G. et al., 2004, A&A, 420, 625
Irstarrfield S., Truran J. W., Sparks W. M., Kutter G. S., 1972, ApJ, 176, 169
Irsteinberg E., Metzger B. D., 2018, MNRAS, 479, 687
Irstrüder L. et al., 2001, A&A, 365, L18
Ivanova N. et al., 2013, A&AR, 21, 59
Ivinson R. J., Hughes D. H., Lloyd H. M., Bang M. K., Bode M. F., 1993, MNRAS, 263, L43
Izzo L. et al., 2018, Astron. Telegram, 11468, 1
Jansen F. et al., 2001, A&A, 365, L1
Jean P., Cheung C. C., Ojha R., van Zyl P., Angioni R., 2018, Astron. Telegram, 1, 11546
Jose J., 2016, Stellar Explosions: Hydrodynamics and Nucleosynthesis. CRC Press/Taylor and Francis
Joye W. A., Mandel E., 2003, New Features of SAOImage DS9, ASPC vol. 295, p. 489
Kahabka P., van den Heuvel E. P. J., 1997, ARA&A, 35, 69
Kalberla P. M. W., Burton W. B., Hartmann D., Arnal E. M., Bajaja E., Morras R., Pöppel W. G. L., 2005, A&A, 440, 775
Kato M., Hachisu I., 1994, ApJ, 437, 802
Kato M. et al., 2016, ApJ, 830, 40
Kellogg E., Baldwin J. R., Koch D., 1975, ApJ, 199, 299
Kimeswenger S., Dalnodar S., Knapp A., Schafer J., Unterguggenberger S., Weiss S., 2008, A&A, 479, L51
Kochanek C. S. et al., 2017, PASP, 129, 104502
Kovetz A., Prialnik D., 1985, ApJ, 291, 812
Krautter J., 2002, in Hernanz M., José J., eds, AIP Conf. Ser. Vol. 637, Classical Nova Explosions. Astron. Soc. Pac., San Fransisco, p. 345
Krautter J., 2008, in Bode M. F., Evans A., eds, Cambridge Astrophysics Series, No. 43. Cambridge University Press, Cambridge, p. 232

Kuschnig R. et al., 2018, Astron. Telegram, 11508, 1
Liedahl D. A., Osterheld A. L., Goldstein W. H., 1995, ApJ, 438, L115
Li F., Zhu C., Lü G., Wang Z., 2016, PASJ, 68, 39
Li K.-L. et al., 2017, Nat. Astron., 1, 697
Li K. L. et al., 2012, ApJ, 761, 99
Linford J. D. et al., 2015, ApJ, 805, 136
Livio M., Mastichiadis A., Oegelman H., Truran J. W., 1992, ApJ, 394, 217
Livio M., Shankar A., Burkert A., Truran J. W., 1990, ApJ, 356, 250
Livio M., Truran J. W., 1994, ApJ, 425, 797
Lodders K., 2003, ApJ, 591, 1220
Luckas P., 2018, Astron. Telegram, 11460
Lynch D. K. et al., 2008, AJ, 136, 1815
Madsen K. K. et al., 2015, ApJS, 220, 8
Martin P., Dubus G., Jean P., Tatischeff V., Dosne C., 2018, A&A, 612, A38
Martínez-Núñez S. et al., 2017, Space Sci. Rev., 212, 59
Mason E., Shore S. N., De Gennaro Aquino I., Izzo L., Page K., Schwarz G. J., 2018, ApJ, 853, 27
Mason E., Walter F. M., 2014, Lesson Learned from (some) Recurrent Novae, ASPC vol. 490, p. 199
Mason K. O. et al., 2001, A&A, 365, L36
Mattox J. R. et al., 1996, ApJ, 461, 396
McLaughlin D. B., 1944, Pop. Astron., 52, 109
McLoughlin D., Blundell K. M., Lee S., 2020, MNRAS, 494, 743
Merloni A. et al., 2012, preprint (arXiv:1209.3114)
Metzger B. D., Caprioli D., Vurm I., Beloborodov A. M., Bartos I., Vlasov A., 2016, MNRAS, 457, 1786
Metzger B. D., Finzell T., Vurm I., Hascoët R., Beloborodov A. M., Chomiuk L., 2015, MNRAS, 450, 2739
Metzger B. D., Hascoët R., Vurm I., Beloborodov A. M., Chomiuk L., Sokoloski J. L., Nelson T., 2014, MNRAS, 442, 713
Mewe R., Gronenschild E. H. B. M., van den Oord G. H. J., 1985, A&AS, 62, 197
Molaro P., Izzo L., Mason E., Bonifacio P., Della Valle M., 2016, MNRAS, 463, L117
Morii M., Yamaoka H., Mihara T., Matsuoka M., Kawai N., 2016, PASJ, 68, S11
Morii M. et al., 2013, ApJ, 779, 118
Mukai K., 2017, PASP, 129, 062001
Mukai K., Ishida M., 2001, ApJ, 551, 1024
Mukai K. et al., 2014, in Woudt P. A., Ribeiro V. A. R. M., eds, ASP Conf. Ser. Vol. 490, Stellar Novae: Past and Future Decades. Astron. Soc. pac., San Fransisco, p. 327
Munari U., Hambsch F.-J., Frigo A., 2017, MNRAS, 469, 4341
Negoro H. et al., 2016, PASJ, 68, S1
Nelson T., Donato D., Mukai K., Sokoloski J., Chomiuk L., 2012, ApJ, 748, 43
Nelson T., et al., 2020, preprint (arXiv:2007.15702)
Nelson T., Mukai K., Sokoloski J. L., Metzger B., Chomiuk L., Linford J., Vurm I., 2018, Astron. Telegram, 11608, 1
Nelson T., Orio M., Cassinelli J. P., Still M., Leibowitz E., Mucciarelli P., 2008, ApJ, 673, 1067
Nelson T. et al., 2014, ApJ, 785, 78
Nelson T. et al., 2019, ApJ, 872, 86
Nemeth P., 2010, PhD thesis, Florida Institute of Technology
Ness J.-U., Schwarz G. J., Retter A., Starrfield S., Schmitt J. H. M. M., Gehrels N., Burrows D., Osborne J. P., 2007, ApJ, 663, 505
Ness J.-U., Starrfield S., Jordan C., Krautter J., Schmitt J. H. M. M., 2005, MNRAS, 364, 1015
Ness J.-U. et al., 2009, AJ, 137, 3414
Ness J. U., 2012, Bull. Astron. Soc. India, 40, 353
O'Brien T. J., Lloyd H. M., Bode M. F., 1994, MNRAS, 271, 155
Orio M., Rana V., Page K. L., Sokoloski J., Harrison F., 2015, MNRAS, 448, L35
Orio M. et al., 2001, MNRAS, 326, L13
Orlando S., Drake J. J., 2012, MNRAS, 419, 2329
Owocki S. P., Castor J. I., Rybicki G. B., 1988, ApJ, 335, 914
O'Brien T. J., Bode M. F., 2008, in Bode M. F., Evans A., eds, Cambridge Astrophysics Series, No. 43, Cambridge University Press, Cambridge, p. 285
Pablo H. et al., 2016, PASP, 128, 125001
Page K. L., Beardmore A. P., Osborne J. P., 2019, preprint (arXiv:1908.02004)
Page K. L., Osborne J. P., Wagner R. M., Beardmore A. P., Shore S. N., Starrfield S., Woodward C. E., 2013, ApJ, 768, L26
Page K. L. et al., 2015, MNRAS, 454, 3108
Pastorello A. et al., 2019, A&A, 630, A75
Pavana M., Raj A., Bohlsen T., Anupama G. C., Gupta R., Selvakumar G., 2020, MNRAS, 495, 2075
Pejcha O., Metzger B. D., Tomida K., 2016, MNRAS, 461, 2527
Peretz U., Orio M., Behar E., Bianchini A., Gallagher J., Rauch T., Tofflemire B., Zemko P., 2016, ApJ, 829, 2
Piano G. et al., 2018, Astron. Telegram, 11553, 1
Poggiani R., 2018, preprint (arXiv:1803.11529)
Popowicz A. et al., 2017, A&A, 605, A26
Poznanski D., Prochaska J. X., Bloom J. S., 2012, MNRAS, 426, 1465
Predehl P. et al., 2016, in Space Telescopes and Instrumentation 2016: Ultraviolet to Gamma Ray, Proceedings of the SPIE, Volume 9905, p. 99051K
Rabus M., Prieto J. L., 2018, Astron. Telegram, 11506, 1
Rauch T., Orio M., Gonzales-Riestra R., Nelson T., Still M., Werner K., Wilms J., 2010, ApJ, 717, 363
Ribeiro V. A. R. M. et al., 2014, ApJ, 792, 57
Richards A. M. S., Etoka S., Gray M. D., Lekht E. E., Mendoza-Torres J. E., Murakawa K., Rudnitskij G., Yates J. A., 2012, A&A, 546, A16
Rohrbach J. G., Ness J.-U., Starrfield S., 2009, AJ, 137, 4627
Roming P. W. A. et al., 2005, Space Sci. Rev., 120, 95
Roy N. et al., 2012, Bull. Astron. Soc. India, 40, 293
Rupen M. P., Mioduszewski A. J., Sokoloski J. L., 2008, ApJ, 688, 559
Ryder S. D., Kool E. C., Chomiuk L., 2018, Astron. Telegram, 11504, 1
Sala G., Hernanz M., Ferri C., Greiner J., 2010, in Comastri A., Angelini L., Cappi M., eds, AIP Conf. Ser. Vol. 1248, X-ray Astronomy 2009; Present Status, Multi-Wavelength Approach and Future Perspectives. Am. Inst. Phys., New York, p. 197
Schlafly E. F., Finkbeiner D. P., 2011, ApJ, 737, 103
Schultz G. V., Wiemer W., 1975, A&A, 43, 133
Schwarz G. J., Shore S. N., Starrfield S., Hauschildt P. H., Della Valle M., Baron E., 2001, MNRAS, 320, 103
Schwarz G. J. et al., 2011, ApJS, 197, 31
Seaquist E. R., Bode M. F., 2008, in Bode M. F., Evans A., eds, Cambridge Astrophysics Series, No. 43, Cambridge University Press, Cambridge, p. 141
Seaquist E. R., Taylor A. R., 1990, ApJ, 349, 313
Shappee B. J. et al., 2014, ApJ, 788, 48
Shara M. M., Prialnik D., Hillman Y., Kovetz A., 2018, ApJ, 860, 110
Shara M. M. et al., 2017, ApJ, 839, 109
Shaviv N. J., 2001a, MNRAS, 326, 126
Shaviv N. J., 2001b, ApJ, 549, 1093
Shore S. N., De Gennaro Aquino I., Schwarz G. J., Augusteijn T., Cheung C. C., Walter F. M., Starrfield S., 2013, A&A, 553, A123
Siegert T. et al., 2018, A&A, 615, A107
Slane P., Bykov A., Ellison D. C., Dubner G., Castro D., 2015, Space Sci. Rev., 188, 187
Sokolovsky K. V. et al., 2017, MNRAS, 464, 274
Stanek K. Z. et al., 2018, Astron. Telegram, 11454
Starrfield S., Iliadis C., Hix W. R., 2008, in Bode M. F., Evans A., eds, Cambridge Astrophysics Series, No. 43. Cambridge University Press, Cambridge, p. 77
Starrfield S., Iliadis C., Hix W. R., 2016, PASP, 128, 05100f
Steinberg E., Metzger B. D., 2020, MNRAS, 491, 4232
Steiner J. E., Campos R., Cieslinski D., 1999, IAU Circ., 7185, 2
Strader J., Chomiuk L., Holoien T. W. S., Prieto J. L., Stanek K. Z., Shappee B. J., Dong S., 2018, Astron. Telegram, 11456, f
Sundqvist J. O., Owocki S. P., Puls J., 2018, A&A, 611, A17
Suzuki A., Shigeyama T., 2010, ApJ, 723, L84

Takei D., Ness J.-U., Tsujimoto M., Kitamoto S., Drake J. J., Osborne J. P., Takahashi H., Kinugasa K., 2011, PASJ, 63, S729
Takei D., Tsujimoto M., Kitamoto S., Ness J.-U., Drake J. J., Takahashi H., Mukai K., 2009, ApJ, 697, L54
Tamuz O., Mazeh T., North P., 2006, MNRAS, 367, 1521
Tavani M. et al., 2008, Nucl. Instrum. Methods Phys. Res. A, 588, 52
Tavani M. et al., 2009, A&A, 502, 995
Thompson D. J. et al., 1993, ApJS, 86, 629
Toumilovitch O., Blane D., Rijsdijk C., 2018, Mon. Notes Astron. Soc. South. Afr., 77, 25
Truran J. W., Livio M., 1986, ApJ, 308, 721
Turner M. J. L. et al., 2001, A&A, 365, L27
van den Bergh S., Younger P. F., 1987, A&AS, 70, 125
Vanlandingham K. M., Schwarz G. J., Shore S. N., Starrfield S., Wagner R. M., 2005, ApJ, 624, 914
Vlasov A., Vurm I., Metzger B. D., 2016, MNRAS, 463, 394
Vurm I., Metzger B. D., 2018, ApJ, 852, 62
Wall J. V., Jenkins C. R., 2003, Cambridge observing handbooks for research astronomers, Vol. 3. Cambridge University Press, Cambridge, UK
Walter F. M., Battisti A., 2011, in American Astronomical Society Meeting Abstracts #217, p. 338.11
Weiss W. W. et al., 2014, PASP, 126, 573
Wendeln C., Chomiuk L., Finzell T., Linford J. D., Strader J., 2017, ApJ, 840, 110
Weston J. H. S., 2016, PhD thesis, Columbia University
Weston J. H. S. et al., 2016a, MNRAS, 457, 887
Weston J. H. S. et al., 2016b, MNRAS, 460, 2687
Williams R., 2016, in Journal of Physics Conference Series, Volume 728, Issue 4, p. 042001
Williams R. E., 1985, in Danziger I. J., Matteucci F., Kjar K., eds, ESO Workshop on Production and Distribution of C, N, O Elements, Garching, West Germany, May 13-15, 1985, Proceedings (A86-47551 23-90) , Garching, West Germany, European Southern Observatory, p. 225
Williams R. E., 1992, AJ, 104, 725
Williams R. E., 1994, ApJ, 426, 279
Wilms J., Allen A., McCray R., 2000, ApJ, 542, 914
Wolf W. M., 2017, PhD thesis, University of California
Wolf W. M., Bildsten L., Brooks J., Paxton B., 2013, ApJ, 777, 136
Yaron O., Prialnik D., Shara M. M., Kovetz A., 2005, ApJ, 623, 398
Zacharias N. et al., 2010, AJ, 139, 2184

APPENDIX A: ESTIMATES OF INNER/OUTER SHELL VELOCITY RATIO FOR THE 'HUBBLE FLOW' MODEL OF NOVA EJECTA

Estimates of $v_{\rm min}/v_{\rm max}$ ratio can be derived from modelling the multifrequency radio light curve of thermal emission from a nova (see Hjellming et al. 1979; Seaquist & Bode 2008; Weston 2016 and appendix A in Finzell et al. 2018). Ribeiro et al. (2014) discussed the effects of the expected bipolar (dumbbell-shaped) geometry of the ejecta on the results of fitting the radio light curves with the simple spherically symmetric 'Hubble flow' model. They found that the spherical model fits overpredict the ejecta mass by up to a factor of 2 and underpredict the shell thickness (proportional to the $v_{\rm min}/v_{\rm max}$ ratio) by up to an order of magnitude (so $v_{\rm min}$ should be close to $v_{\rm max}$). The magnitude of the discrepancy between the spherical and bipolar models depends mostly on the departure from spherical symmetry and only weakly on inclination. The clumpiness of the nova ejecta is an additional source of uncertainty in modelling (Roy et al. 2012). Shocks within the nova ejecta producing thermal (Metzger et al. 2014) and synchrotron (Vlasov et al. 2016; Steinberg & Metzger 2020) emission may further complicate modelling of nova radio light curves. Table A1 summarizes the $v_{\rm min}/v_{\rm max}$ values reported in the literature.

Table A1. The inner/outer shell velocity ratios from the literature.

Nova	$v_{\rm min}/v_{\rm max}$	Reference
V1324 Sco	$0.447^{+0.10}_{-0.079}$	Finzell et al. (2018)
V959 Mon	0.083	Chomiuk et al. (2014a)
V5589 Sgr	0.84	Weston et al. (2016b)
V1723 Aql	0.17	Weston et al. (2016a)
T Pyx	0.25	Nelson et al. (2014)
V723 Cas	0.24 ± 0.1	Heywood et al. (2005)
V1974 Cyg	0.46[a]	Hjellming (1996)
V351 Pup	0.74[b]	Wendeln et al. (2017)
V838 Her	0.042	Hjellming (1996)
V827 Her	0.25	Hjellming (1996)
V1819 Cyg	0.2	Hjellming (1996)
QU Vul	0.87	Hjellming (1996)
V1500 Cyg	0.036	Hjellming et al. (1979)
FH Ser	0.048	Hjellming et al. (1979)
HR Del	0.44	Hjellming et al. (1979)

[a]Ivinson et al. (1993) report $v_{\rm min}/v_{\rm max} = 0.16$.
[b]Hjellming (1996) found $v_{\rm min}/v_{\rm max} = 0.069$.
Column designation: Column 1 – Nova name; Column 2 – The velocity ratio derived from the 'Hubble flow' model; Column 3 – Citation.

This paper has been typeset from a TEX/LATEX file prepared by the author.